

## An ecohydrological approach to predicting hillslope-scale vegetation patterns in dryland ecosystems

Trenton E. Franz,<sup>1</sup> Kelly K. Caylor,<sup>2</sup> Elizabeth G. King,<sup>3</sup> Jan M. Nordbotten,<sup>2,4</sup> Michael A. Celia,<sup>2</sup> and Ignacio Rodríguez-Iturbe<sup>2</sup>

Received 6 February 2011; revised 24 November 2011; accepted 13 December 2011; published 18 January 2012.

[1] Drylands are an important ecosystem, as they cover over 40% of the Earth's land surface and are believed to be sensitive to climate change. Where dryland vegetation supports pastoralist livestock production, catastrophic ecological shifts present a grave concern because of the direct coupling between the quality of available forage and human livelihoods. In this research we investigate the organization of vegetation on hillslopes by developing a relatively simple spatially explicit daily stochastic ecohydrological model. Using a 2 year observational study in central Kenya, we present an empirical patch water balance of three representative patch types, bare soil, grass, and tree. Given the recent expansion of bare areas, the system is dominated by Hortonian runoff and overland flow. By incorporating concepts of simple local interactions from complex systems we are able to simulate a range of surface flowpath convergence states across the hillslope during a rain event. The model also allows the root to canopy radius of the tree patches to vary affecting the length scale of water competition. By changing the length scales of facilitation and competition, the model demonstrates a range of most efficient hillslope water-use patterns from random to highly organized static vegetation patterns. The findings of this work support the mechanism of symmetry-breaking instabilities for pattern formation in drylands.

**Citation:** Franz, T. E., K. K. Caylor, E. G. King, J. M. Nordbotten, M. A. Celia, and I. Rodríguez-Iturbe (2012), An ecohydrological approach to predicting hillslope-scale vegetation patterns in dryland ecosystems, *Water Resour. Res.*, 48, W01515, doi:10.1029/2011WR010524.

### 1. Introduction

[2] The health of arid and semiarid lands is a critical challenge, as these ecosystems cover ~41% of the Earth's land surface and contain 38% of the human population [Reynolds et al., 2007]. The majority of traditional pastoralist societies exist in these ecosystems [Sankaran et al., 2005]. The sustainability of these societies is particularly vulnerable to catastrophic shifts in vegetation structure because of the direct coupling of vegetation condition and basic human sustenance [Fratkin and Mearns, 2003; Kefi et al., 2007; Rietkerk et al., 1996]. In addition, global climate change is anticipated to have significant impacts on future rainfall patterns in dryland ecosystems, affecting both the mean and variance [Meehl et al., 2007], further increasing the potential for catastrophic vegetation shifts.

[3] The threat of catastrophic shifts in these systems and the diverse pattern development of natural vegetation have sparked scientific interest into the principles that govern

dryland vegetation patterns [Borgogno et al., 2009; Rietkerk and Van de Koppel, 2008; Scanlon et al., 2007; Sole, 2007; Turnbull et al., 2008]. Given the natural control of water limitation in these ecosystems [Rodríguez-Iturbe and Porporato, 2004], theories of self-organization are often invoked to explain the emergent patterns [Caylor et al., 2009; Eagleson, 1982; Hwang et al., 2009; Kerkhoff et al., 2004; Schymanski et al., 2008]. In addition, development of mathematical models that incorporate the physical mechanism of symmetry-breaking instabilities [Borgogno et al., 2009] can recreate the diverse set of spatial patterns that may emerge. The resulting periodic and scale-free distribution patterns that emerge [Manor and Shnerb, 2008; von Hardenberg et al., 2010] have been hypothesized to indicate signatures of imminent desertification in drylands [Barbier et al., 2006; Kefi et al., 2007; Scanlon et al., 2007; Sole, 2007]. While the mathematical models are able to recreate the emergent patterns, experimental measurements in natural ecosystems justifying the use of symmetry-breaking instabilities are often lacking [Barbier et al., 2008; Borgogno et al., 2009].

[4] Of particular importance to dryland ecosystems is the coupling of surface and subsurface flow processes [Istanbuloglu and Bras, 2005, 2006]. Depending on the spatial and temporal scale of interest, physical models may require a nontrivial amount of computer resources [Ivanov et al., 2008], and datasets for model parameterization and validation are often not possible to obtain [Vereecken et al., 2008]. While a full coupling of the physical processes is

<sup>1</sup>Department of Hydrology and Water Resources, University of Arizona, Tucson, Arizona, USA.

<sup>2</sup>Department of Civil and Environmental Engineering, Princeton University, Princeton, New Jersey, USA.

<sup>3</sup>Department of Ecology and Evolutionary Biology, Princeton University, Princeton, New Jersey, USA.

<sup>4</sup>Department of Mathematics, University of Bergen, Bergen, Norway.

possible [Furman, 2008], the stochastic nature of rainfall forcing in drylands [Katul et al., 2007] often makes solutions intractable at larger spatial and longer temporal scales. In order to address this issue, parsimonious models capturing the general behavior of the system have been proposed that yield analytical solutions [D'Odorico et al., 2006; Isham et al., 2005; Laio et al., 2001]. However, the limits of analytical models often do not extend beyond idealized conditions that are not always representative of processes that govern natural systems.

[5] The purpose of the current work is to investigate the processes that affect the organization of vegetation at the spatial scale of hillslopes. Using observations from a dryland ecosystem in central Kenya, we construct a parsimonious spatially explicit daily ecohydrological model that is able to demonstrate a range of vegetation patterns observed across this ecosystem. Of particular importance in this ecosystem and many dryland ecosystems [Newman et al., 2006], is the effect of redistribution of surface waters to downslope vegetation patches as a result of Hortonian runoff and overland flow. The influence of runoff-runoff dynamics has been exacerbated in recent years in this ecosystem by the expansion of bare soils due to overgrazing, with the changes leading to the proliferation of an undesirable succulent plant that threatens the sustainability of this pastoralist ecosystem [King et al., 2012].

[6] Due to the nature of overland flow and ubiquity of surface flow paths on hillslopes [Dingman, 2002]; explicit treatment of individual flow paths is impractical at larger spatial scales. While previous studies have coupled runoff-runoff dynamics with sediment transport processes [Saco et al., 2007], idealized geometry [Thompson et al., 2010], and probabilistic modeling [Manfreda et al., 2009], we use a rule-based method based on a complex adaptive systems approach [Harte, 2002; Levin, 1998] to generate the basic patterns. In order to compare different possible static spatial vegetation patterns that exist, we constrain the hillslope model to the growing season water balance. Using the dryland resource trade-off hypothesis proposed by [Caylor et al., 2009], we are able to compare the different static patterns according to their hillslope water use efficiency. Starting with the same initial conditions and simulating a series of growing season daily precipitation events, we evaluate the changes in the growing season water balance between different static spatial patterns of vegetation with the same fractional cover. In addition, we vary the strength of the local facilitation and long-range competition effects by varying the model parameters that control the effectiveness of surface flowpath convergence and root to canopy ratios, respectively. By changing these two parameters we are able to demonstrate a range of most efficient static spatial patterns from highly organized to random, which maximizes hillslope water use efficiency. We compare the most efficient modeled spatial patterns and different fractional covers with high-resolution satellite imagery of the study site.

[7] The remainder of the paper is organized as follows. In section 2 we describe the study site in central Kenya, our observational study, hillslope water balance, and estimation of hillslope water use efficiency. Section 3 presents the observational study results, model validation and sensitivity analysis, and observed and modeled patterns of hillslope vegetation spatial clustering. In Section 4 we describe the

hillslope spatial clustering comparison and the role of facilitation and competition in creating emergent vegetation patterns in this dryland ecosystem. The remainder of the paper is devoted to identifying limitations of the current study that should be addressed with future work.

## 2. Methodology

### 2.1. Observational Study

[8] Our observational study site ( $0^{\circ}31'22''\text{N}$ ,  $36^{\circ}55'36''\text{E}$ ) is located in the Upper Ewaso Ng'iro River basin on the central Kenya highlands (Figure 1a). Details about the basin's general climate, soils, and vegetation are provided elsewhere [Franz et al., 2010], with parameters at the observational study site summarized in Tables 1 and 2. The study site is located in Koiya Group Ranch, which is communally owned by resident Laikipia Maasai people. The study site has well-defined basins between 1 and 15 km<sup>2</sup>, where individual basins have typical slopes between 3 and 7° with maximum hillslope lengths ranging between 0.5 and 2 km (Figure 1b). Fractional cover of vegetation was determined using a 4.8 km × 14.7 km Quickbird image (Digitalglobe, Inc. Longmont, CO, resolution 0.77 m × 0.77 m) of the study area, taken on 23 May 2007, at the end of the primary growing season. The image was divided into 400 × 400 m sections, and each pixel underwent unsupervised classification as bare, grass, or tree (K. Guan et al., Multi-sensor synthesis of vegetation pattern over a large climatic gradient transect in Africa, manuscript in preparation, 2012) (Figure 1c). Mean bare soil fractional cover in 400 m × 400 m areas was 53.2% (standard deviation = 16.8%), grass 19.7% (7.07%), and tree 26.9% (14.1%). In addition to the remote sensing image, individual trees were mapped and characterized (including species, height, and canopy dimensions), in twenty-seven 1-ha plots around the study area (Table 3) (A. Lester, unpublished data, 2008). Table 3 illustrates that *Acacia etbaica*, *A. mellifera*, and *A. tortilis* are the three dominant species in the study area and locally dominant within individual plots. The three species had similar height (1 to 3 m) and canopy crown sizes (2 to 16 m<sup>2</sup>) among the plots surveyed. A Poisson analysis of individual tree clustering (Lester, unpublished data), indicated that trees tended to be more aggregated in 14 of the 21 plots analyzed and the tendency to cluster was not explained by variations in mean slope, elevation, species abundance, or tree density.

[9] Beginning in February 2007 and ending in December 2008, a series of data logging sensors were used to determine rainfall, soil moisture, and surface runoff for three different representative patch types; bare soil, grass, and tree (*A. tortilis*) with grass. We selected one patch of each type occurring in a 30 m radius area, located at the mid-slope in an arbitrarily selected basin with a mean slope of 5°. We installed a tipping bucket rain gauge (TE525, Campbell Scientific Inc., Logan, UT), and in each patch installed time domain reflectometry (TDR) soil moisture sensors at 5, 10, 20, 30, and 70 cm depth, oriented horizontally (CS616, Campbell Scientific Inc., Logan, UT); data were collected every 10 min. We present the data as aggregated daily values and average the soil moisture measurements for a value representative of the top 40 cm. We calibrated each CS616 probe with volumetric soil moisture samples collected at 15 and 30 cm in July 2007 and April 2008

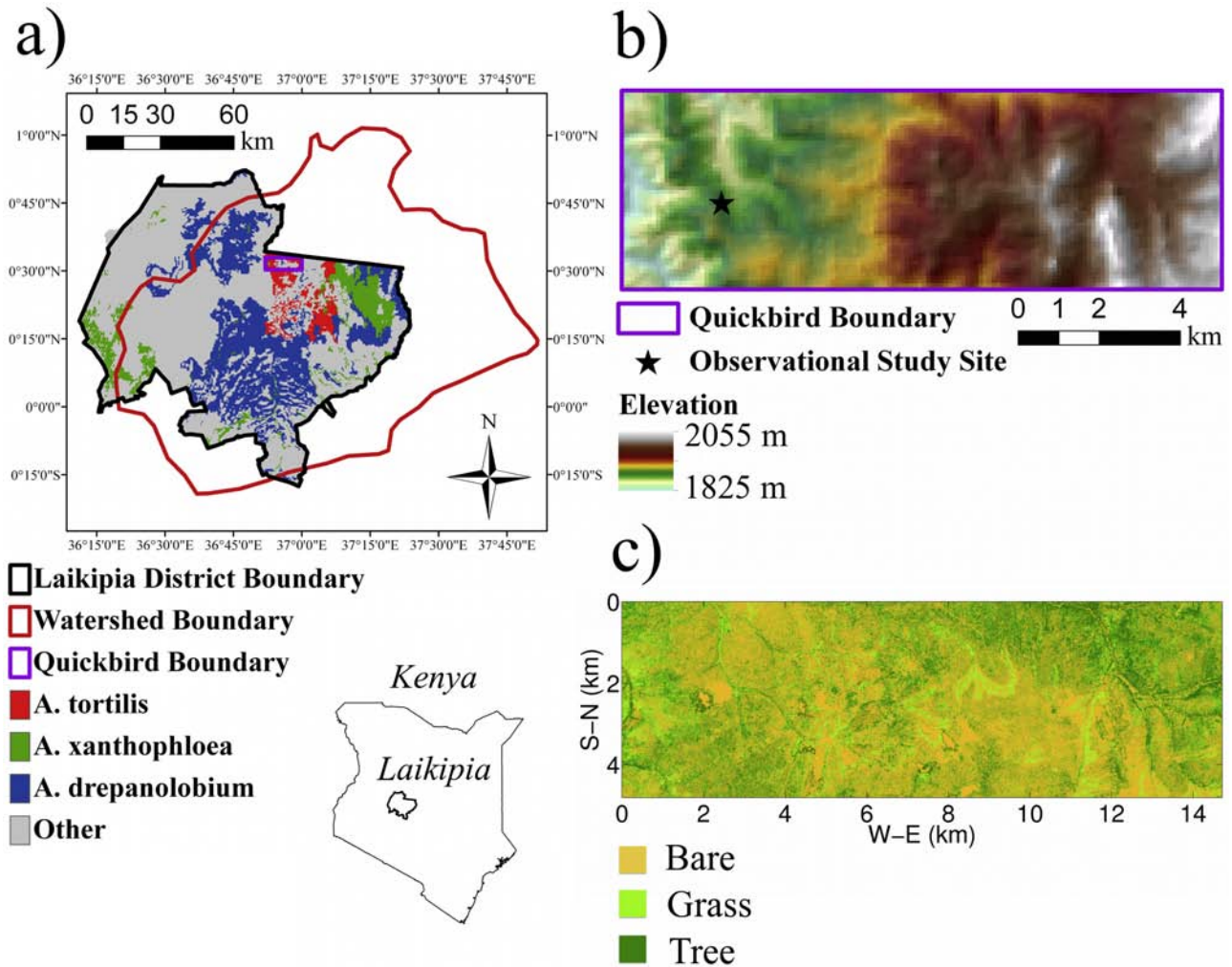


**Figure 1.** (a) Location map of study area in central Kenya illustrating political boundaries, watershed boundary, Quickbird imagery boundary, and distribution of three most abundant *Acacia* tree species [Franz *et al.*, 2010], (b) digital elevation map (90 m resolution) of study area, and (c) distribution of bare, grass, and trees from reclassification of satellite imagery (Guan *et al.*, 2012, in preparation).

following [Kelleners *et al.*, 2005]. We quantified surface runoff in each of the three patch types with a constructed  $4\text{ m} \times 4\text{ m}$  gutter and rail system. The rail was buried 10 cm in the ground and extended 10 cm above the surface on three sides. The gutter was placed perpendicular to the downslope direction and buried 5 cm in the ground to capture surface runoff inside the plot. A wire mesh was used to prevent debris flow into the gutter and was periodically cleaned during the experiment. The captured runoff water was collected in 1000 L tanks where the height of the water was recorded with a pressure transducer (CS408, Campbell Scientific Inc., Logan, UT), at 10 min intervals. The water level data was aggregated to daily values. We analyzed all storm event data at the daily timescale and patch water-use data at the interstorm timescale between rain events.

## 2.2. Hillslope Water Balance

[10] A fully coupled dynamic vegetation, energy, and water balance model is not a trivial problem to solve for the spatial and temporal scales of seasonal vegetation response on hillslopes. Depending on system physics,

fluxes may be connected both locally and across the entire domain, adding to the complexity of the problem solution. Because we are primarily motivated by differences in seasonal landscape water use, we constructed a relatively simple spatially explicit modeling framework at the daily timescale. The model is a two-dimensional, vertically averaged model with the primary state variable being the daily volumetric water content  $\theta$  ( $\text{m}^3\text{ m}^{-3}$ ) averaged over the top 400 mm of the soil column  $Z_r$  (mm). The individual patches,  $x$ , represent  $4\text{ m} \times 4\text{ m}$  areas identified from the observational study. The basic water balance within each patch,  $x$ , at time  $t$  is determined according to the daily changes in patch soil moisture,  $\theta(x, t)$ , according to

$$\frac{\Delta\theta(x, t)}{\Delta t} Z_r = I(x, t) - L(x, t) - ET(x, t), \quad (1)$$

where  $I$  ( $\text{mm d}^{-1}$ ) is the daily infiltration rate,  $L$  ( $\text{mm d}^{-1}$ ) is the daily vertical leakage rate, and  $ET$  ( $\text{mm d}^{-1}$ ) is the daily evapotranspiration rate (Table 2). Volumetric water content and relative saturation,  $s$  (%), are used interchangeably

**Table 1.** Summary of Growing Season Climate Parameters for Experimental Study Site in Central Kenya at 0°31'22"N, 36°55'36"E<sup>a</sup>

Growing Season Climate Parameters for Kenya	Value
Length of growing season (day) <sup>b</sup>	90
Number of growing seasons per year <sup>b</sup>	2
Total rainfall (mm) <sup>c</sup>	178.2
Coefficient of variation <sup>c</sup>	0.318
Percent of annual rainfall per growing season <sup>c</sup>	35
Mean daily storm depth, $\alpha$ (mm) <sup>c</sup>	9
Mean storm arrival rate, $\lambda$ (d <sup>-1</sup> ) <sup>c</sup>	0.22
Average rainfall rate, $i$ (mm h <sup>-1</sup> ) <sup>d</sup>	6.5 (4.24)
Mean daily relative humidity (%) <sup>c</sup>	65 (5)
Mean daily pan evaporation (mm d <sup>-1</sup> ) <sup>c</sup>	6 (2)
Mean daily incoming shortwave radiation (W m <sup>-2</sup> daylight <sup>-1</sup> ) <sup>c</sup>	325 (90)
Mean sunshine hours (h d <sup>-1</sup> ) <sup>c</sup>	6.5 (2.5)
Mean daily temperature (°C) <sup>c</sup>	20 (1.5)
Mean daily wind speed (m s <sup>-1</sup> ) <sup>c</sup>	1.9 (0.5)

<sup>a</sup>Please note that the values reported in parentheses is SD.

<sup>b</sup>Primary growing seasons are March to May and October to December.

<sup>c</sup>Estimated from 50 years of daily (CETRAD/NRM3 of Nanyuki, Kenya).

<sup>d</sup>Estimated from 21 storm events over 2 year experiment measured with tipping bucket rain gauge (10 min intervals).

<sup>e</sup>Estimated from 15 years of daily data (CETRAD/NRM3 of Nanyuki, Kenya).

where they are related by  $s = \frac{\theta}{n}$ , where  $n$  (m<sup>3</sup> m<sup>-3</sup>) is the soil porosity.

[11] The effective rainfall rate onto each patch  $x$  at time  $t$ ,  $P_e(x, t)$ , is determined by considering both the direct precipitation onto patch  $x$  at time  $t$ ,  $P(x, t)$  (mm d<sup>-1</sup>), and the upslope runoff into patch  $x$ ,  $R_u(x, t)$  (mm d<sup>-1</sup>), so that

$$P_e(x, t) = P(x, t) + R_u(x, t). \quad (2)$$

Daily rainfall,  $P(x, t)$ , is characterized as a marked Poisson process with an interstorm arrival rate (d<sup>-1</sup>) of  $\lambda$  and a storm depth (mm) of  $\alpha$ . The rainfall process is further char-

**Table 3.** Summary of Individual Tree Species in Plots Surveyed Inside the Satellite Imagery Study Area

Stem Density <sup>a</sup>	Average (%)	SD (%)
<i>A. drepanolobium</i>	0.08	0.41
<i>A. etbaica</i>	13.27	14.95
<i>A. mellifera</i>	32.50	31.21
<i>A. nilautica</i>	8.61	9.65
<i>A. reficiens</i>	0.91	1.10
<i>A. seyal</i>	3.16	13.38
<i>A. tortilis</i>	39.29	27.75
Non-Acacia	2.18	3.23
<i>Percent Canopy Cover</i>		
All plots	19.90	10.47

<sup>a</sup>Sampled 27 plots around study area, where 21 were 100 m × 100 m, 6 were 50 m × 100 m, and 4802 individual trees were categorized (Lester, unpublished data).

acterized by a daily rainfall intensity,  $i$  (mm h<sup>-1</sup>), which is assumed to be independent of storm depth. The underlying probability distributions of interstorm arrival rate, rainfall depth, and rainfall intensity are all taken to be exponential, with mean values of each distribution derived from observations of the rainfall process within the study basin (Table 1).

[12] The daily patch water balance was separated into three regimes based on the effective precipitation and patch water balance characteristics. No subsurface lateral redistribution of water was considered in this model but its role in this ecosystem is discussed elsewhere [Franz *et al.*, 2011]. The first regime is the interstorm period, when evapotranspiration ( $ET$ ) is occurring. Here the soil moisture solution follows an exponential decay asymptotically approaching the soil hygroscopic point,  $s_h$ , where the decay constants  $k$  (m<sup>3</sup> m<sup>-3</sup> d<sup>-1</sup>) are defined from the observed soil moisture traces for each patch type which are assumed

**Table 2.** Summary of Soil and Vegetation Parameters for Each Patch Type<sup>a</sup>

	Bare	Grass	Tree
Soil depth, $Z_r$ (mm) <sup>b</sup>	400	400	400
Maximum canopy interception, $I_{max}$ (mm) <sup>b</sup>	0	1	2
Maximum evapotranspiration, $E_{max}$ (mm d <sup>-1</sup> ) <sup>c</sup>	7	4	6
Vertical saturated hydraulic conductivity, $K_{sv}$ (mm h <sup>-1</sup> ) <sup>d</sup>	6.6 (0.779)	16.7 (1.53)	14.5 (2.31)
Incipient Hortonian runoff generation, $R_u^i$ (mm) <sup>c</sup>	6	6	6
Porosity, $n$ (m <sup>3</sup> m <sup>-3</sup> ) <sup>f</sup>	0.45	0.45	0.45
Air Entry Pressure, $\psi_{aq}$ (mm) <sup>f</sup>	218	218	218
Pore size index, $b$ (-) <sup>f</sup>	4.9	4.9	4.9
Soil water retention curve, $\psi_{avg}$ (MPa) <sup>g</sup>	-0.0007	-0.0007	-0.0007
Hygroscopic saturation, $s_h$ (%), where $\psi = -10$ MPa) <sup>g</sup>	0.1419	0.1419	0.1419
Field capacity saturation, $s_{fc}$ (%), where $\psi = -0.033$ MPa) <sup>g</sup>	0.4555	0.4555	0.4555
Wilting point saturation, $s_w$ (%), where $\psi = -3$ MPa) <sup>h</sup>	-	0.1815	0.1815
Incipient stomatal closure point saturation, $s_s$ (%), where $\psi = -0.045$ MPa) <sup>h</sup>	-	0.4276	0.4276
Water stress exponent, $q^g$	-	2	2
Evapotranspiration exponential decay constant $k$ , (m <sup>3</sup> m <sup>-3</sup> d <sup>-1</sup> ) <sup>i</sup>	0.0621 (0.0041)	0.0305 (0.0038)	0.0565 <sup>j</sup> (0.0056)
Mean daily patch water use at well watered conditions = $nZ_rks_{fc}$ (mm d <sup>-1</sup> )	5.09	2.50	4.63

<sup>a</sup>Value reported in parenthesis is SE.

<sup>b</sup>Assumed value.

<sup>c</sup>Approximated by Penman-Monteith, Penman-Combination equation, using growing season climate parameters (Table 1) and vegetation characteristics [Franz *et al.*, 2010].

<sup>d</sup>Estimated from 12 samples in each patch type collected with minidisc infiltrometer in July 2007.

<sup>e</sup>Estimated from 21 storm events for 4x4 m runoff plots during 2 year experiment.

<sup>f</sup>Estimated from sandy loam [Clapp and Hornberger, 1978; Dingman, 2002].

<sup>g</sup>Adopted from [Rodríguez-Iturbe and Porporato, 2004].

<sup>h</sup>Estimated from *A. tortilis* [Otieno *et al.*, 2005].

<sup>i</sup>Estimated from 15 inter-storm periods during 2 year experiment.

<sup>j</sup>Value is for combined grass and tree patch. Subtract grass decay constant from this value to obtain tree only decay constant for roots that extend beyond canopy crown.

identical across the domain (Table 2). While the roots in the grass patches do not extend beyond their surface canopy, we allow the tree roots to extend beyond their above-ground canopies defined by the parameter  $RCR$ , which is the root to canopy radius (again assumed identical over the domain for each simulation). Each patch is assigned an effective  $k$  value, which is the sum of fraction of roots multiplied by the patch type decay constant for the contributing neighbors. For the model simulations, we assume the tree roots occupy 50% of its four primary neighbors and 25% of its four diagonal neighbors for an  $RCR$  equal to 2, and tree roots occupy 100% of its four primary neighbors and 50% of its four diagonal neighbors for an  $RCR$  equal to 3. The total evapotranspiration of an individual tree patch is the sum of its own cell's water use and water use from neighboring cells. In addition to evapotranspiration, vertical leakage out of the soil column ( $L$ ) may take place if the daily starting soil moisture values are above field capacity,  $s_{fc}$ . Partitioning of leakage and evapotranspiration is defined by capping the maximum daily evapotranspiration rate of each patch type (Table 2), where the remaining water loss from the soil moisture exponential decay is attributed to leakage.

[13] On rainy days, evapotranspiration from vegetated patches is set to zero for the entire day, based on the assumption that the high relative humidity results in small vapor pressure deficits. Observations from the patch runoff plots indicate a threshold effective precipitation value,  $R_d^*$  (mm), before Hortonian surface runoff is generated (Tables 2 and 4). In addition, we set a maximum canopy interception value,  $I_{max}$  (mm), where the sum of  $I_{max}$  and  $R_d^*$  must be exceeded in order for vegetated patches to generate surface Hortonian runoff to downslope patches,  $R_d$  (mm). We define this as the second regime, where effective precipitation is converted only into interception,  $Int$  (mm), and bare soil evaporation,  $E$  (mm), which we sum together as event losses,  $EL$  (mm). We note that maximum values are near daily average maximum evapotranspiration rates for the study site (Table 2). Again, vertical leakage ( $L$ ) may take place if daily starting saturations are above field capacity. The third regime is when effective precipitation is higher than the sum of incipient runoff generation and maximum canopy interception. Here surface downslope runoff ( $R_d$ ) occurs and significant infiltration ( $I$ ) may occur resulting in higher soil moisture values. Vertical leakage occurs when the depth of the infiltration front exceeds the soil rooting depth. We use a closed form solution of the Green and

Ampt equation [Dingman, 2002; Green and Ampt, 1911] to estimate the infiltration depth allowing us to partition infiltration ( $I$ ) and leakage ( $L$ ) (Table 2).

[14] The upslope runoff onto each patch  $x$  is dependent on the contribution of three upslope patches according to

$$R_u(x, t) = \sum_{j=1}^3 (R_d(j, t) \times f_d(j)), \quad (3)$$

where  $R_d(j, t)$  ( $\text{mm d}^{-1}$ ) is the downslope runoff from one of three upslope patches  $j$  at time  $t$ , and  $f_d(j)$  is the portion of runoff from patch  $j$  that enters the downslope patch  $x$ . Given the relatively steep slopes ( $>3^\circ$ ), we only considered lateral redistribution of surface runoff to the three downslope neighbors.

[15] The values of  $f_d(j)$  are taken to be constant during the model simulations and are determined by the configuration of three downslope patches scaled by the relative contour lengths between adjacent grids in a flat square lattice. Because we were primarily motivated by exploring a range of general convergence and divergence patterns, this simple flat plane assumption was sufficient for our modeling framework. A more rigorous set of flowpath equations can be found in the work of Quinn *et al.* [1991] that includes both the influence of contour lengths and change in slope on surface convergence patterns. Generally in this ecosystem, the greatest fraction of runoff goes directly downslope, but the downslope patch type also impacts these patterns such that greater fractions of runoff enter downslope bare patches, and the smaller fractions enter downslope vegetation patches. This redistribution of surface water is the result of sediment transport processes (accumulation of material on vegetation and scouring of bare patches), which is not explicitly considered in this work but is clearly visible from observations of flowpaths at the study site. Here we use vegetation type as a proxy for local topography and subsequent surface convergence patterns. The parameter  $fr$ , controls the fraction of runoff that enters downslope vegetation patches. Physically, this parameter controls the level of convergence of surface flow paths, with values near 0 resulting in highly convergent flow into connected bare soil patches and values near 0.4 result in neutral flow into all downslope patches. A sensitivity analysis of this parameter will be presented in section 3.3. The full suite of  $f_d$  coefficients for the five possible configurations of three downslope bare ( $b$ ) and vegetated ( $v$ ) patches within the model is

$$b, b, b = v, v, v \left\{ \begin{array}{l} \frac{1}{2(\sqrt{2}+1)}, \\ \frac{1}{2} - \frac{fr}{2}, \\ \frac{fr}{\sqrt{2}}, \\ 1 - fr \left(1 + \frac{1}{\sqrt{2}}\right), \\ -\frac{(4\sqrt{2}+7)(fr-\sqrt{2})}{8\sqrt{2}(\sqrt{2}+1)^2}, \end{array} \right. \left\{ \begin{array}{l} 1 - \frac{1}{(\sqrt{2}+1)}, \\ fr, \\ 1 - \frac{2fr}{\sqrt{2}}, \\ fr, \\ -\frac{(fr-\sqrt{2})(17+12\sqrt{2})}{8\sqrt{2}(\sqrt{2}+1)^2}, \end{array} \right. \left\{ \begin{array}{l} \frac{1}{2(\sqrt{2}+1)}, \\ \frac{1}{2} - \frac{fr}{2}, \\ \frac{fr}{\sqrt{2}}, \\ \frac{fr}{\sqrt{2}}, \\ \frac{fr}{\sqrt{2}} \end{array} \right. \quad (4)$$

For a flat square lattice the relative contour lengths between the four primary faces and diagonal faces are  $1 : \sqrt{2}$ . We define  $\vec{ac}$  to be the primary downslope face contour length and  $\vec{ab}$  and  $\vec{ad}$  to be the left and right diagonal contour lengths. The relative flux partitioning ( $RF$ ) of the primary and diagonal faces are defined as:

$$RF_{\vec{ac}} = \frac{\vec{ab}}{\vec{ac} + \vec{ab}} = \frac{\sqrt{2}}{1 + \sqrt{2}} = 1 - \frac{1}{\sqrt{2} + 1} \quad \text{and} \quad RF_{\vec{ad}} = \frac{\vec{ab}}{\vec{ac} + \vec{ab}} = \frac{\sqrt{2}}{1 + \sqrt{2}} = 1 - \frac{1}{\sqrt{2} + 1}$$

$$RF_{\vec{ad}} = \frac{1}{2} \left( \frac{\vec{ac}}{\vec{ac} + \vec{ab}} \right) = \frac{1}{2} \left( \frac{1}{1 + \sqrt{2}} \right) = \frac{1}{2(\sqrt{2} + 1)}, \quad \text{as}$$

given by the  $f_d$  coefficients in line 1 ( $b, b, b = v, v, v$ ) of equation (4). Assuming a value of  $fr$  and that it accounts for the local contour and slope effects between bare and vegetated patches, we then equally partition the remaining flux to each diagonal face in line 2 ( $b, v, b$ ). Again scaling by the relative contour lengths, we define the diagonal face coefficients in line 3 ( $v, b, v$ ) as  $\frac{fr}{\sqrt{2}}$ , with the middle coefficient set as the remainder. From our previous definitions the middle and right diagonal coefficients are defined in line 4 ( $b, v, v$ ), with the left diagonal coefficient equaling the remainder. The right diagonal coefficient in line 5 ( $b, b, v$ ) is previously defined, and we partition the remaining flux to the other two coefficients by scaling their relative contour lengths and including one higher order term, where the primary face coefficient is:

$$RF_{\vec{ac}} = \left(1 - \frac{fr}{\sqrt{2}}\right) \left(\frac{\sqrt{2}}{(\sqrt{2} + 1)}\right) + \left(1 - \frac{fr}{\sqrt{2}}\right) \left(\frac{1}{2(\sqrt{2} + 1)}\right)$$

$$\times \left( \left(\frac{\sqrt{2}}{(\sqrt{2} + 1)}\right) + \left(\frac{1}{4(\sqrt{2} + 1)}\right) \right)$$

$$= -\frac{(fr - \sqrt{2})(17 + 12\sqrt{2})}{8\sqrt{2}(\sqrt{2} + 1)^2}$$

and the left diagonal face coefficient is

$$RF_{\vec{ad}} = \left(1 - \frac{fr}{\sqrt{2}}\right) \left(\frac{1}{2(\sqrt{2} + 1)}\right) + \left(1 - \frac{fr}{\sqrt{2}}\right) \left(\frac{1}{2(\sqrt{2} + 1)}\right)$$

$$\times \left( \left(\frac{1}{2(\sqrt{2} + 1)}\right) + \left(\frac{1}{4(\sqrt{2} + 1)}\right) \right)$$

$$= -\frac{(4\sqrt{2} + 7)(fr - \sqrt{2})}{8\sqrt{2}(\sqrt{2} + 1)^2}$$

[16] In each patch, the downslope runoff ( $R_d$ ) generated is characterized using an empirical model derived from two years of rainfall and runoff observations (21 total rainfall events) collected at the study site (Table 4). The resulting relationship takes the form of a general exponential model

$$R_d(P_e, i) = \left[ C_0^R + C_1^R \ln(P_e) + C_2^R \ln(i) + C_3^R \left( (\ln(P_e) - 2.4449) \times (\ln(i) - 1.6661) \right) \right]^2, \quad (5)$$

**Table 4.** Summary of Total Rainfall, Rainfall Intensity, and Total Plot Runoff of 4 m  $\times$  4 m, From 25 Storm Events over 2 Year Experiment Period for Each Patch Type

Daily Rainfall (mm)	Average Rain Rate (mm h <sup>-1</sup> )	Total Runoff (mm), Bare Soil	Total Runoff (mm), Grass	Total Runoff (mm), Tree
6.6	5.7	4.3	1.3	0.7
7.8	- <sup>a</sup>	0.8	0.1	0.2
6.2	- <sup>a</sup>	2.1	0.9	0.3
65.0	- <sup>a</sup>	42.5	37.2	27.0
32.9	8.0	25.2	19.1	20.6
1.5	3.0	0.1	0.0	0.2
1.8	3.6	0.0	0.0	0.1
26.4	6.1	8.6	3.8	3.8
24.4	7.0	15.1	8.7	11.6
15.7	7.1	6.9	3.6	3.0
2.0	2.0	0.1	0.0	0.2
19.9	4.7	10.0	4.4	8.6
44.2	4.5	18.8	10.8	8.7
18.5	14.4	12.2	11.0	11.2
28.6	9.6	12.8	9.0	8.0
12.5	7.5	7.8	4.8	4.5
4.4	2.7	0.4	0.2	0.7
24.2	7.3	12.0	9.8	8.7
35.0	20.2	- <sup>b</sup>	13.4	18.3
7.9	5.2	0.3	0.3	0.5
12.6	10.1	5.6	4.7	4.6
15.4	4.8	5.6	2.7	8.6
4.0	2.1	0.3	0.0	0.5
80.0	7.9	43.9	44.0	34.7
5.5	2.9	0.4	0.1	0.6

<sup>a</sup>Tipping bucket rain gauge malfunctioned, total estimated from wedge gauge.

<sup>b</sup>Pressure transducer in tank malfunctioned.

where  $C_0^R - C_3^R$  are coefficients determined from least-squares regression of the field data for each patch type (either bare or vegetated), effective rainfall is determined in each patch  $x$  at time  $t$  ( $P_e(x, t)$ ), and daily rainfall intensity is constant across all patches ( $i(t)$ ) determined only by the stochastic rainfall process (Table 5). We note that travel time, flow velocity, and residence time are not explicitly modeled across the individual patches and refer to other models for explicit treatment of these processes [Furman, 2008]. Multivariate linear regression indicated minimal dependency of antecedent moisture conditions on runoff production.

[17] The daily water stress,  $\xi(t)$ , of each vegetation patch is [Rodríguez-Iturbe and Porporato, 2004]

$$\xi(t) = \begin{cases} 0 & s(t) > s_* \\ \left( \frac{s_* - s(t)}{s_* - s_w} \right)^q & s_w \leq s(t) \leq s_* \\ 1 & s(t) < s_w \end{cases}, \quad (6)$$

**Table 5.** Summary of Multivariate Linear Regression Runoff Model Coefficients for Each Patch Type Estimated From Storm Events in Table 4 Using Stepwise Multivariate Linear Regression

Coeff.	Bare	Grass	Tree
$C_0^R$	-2.3241	-3.3893	-2.6296
$C_1^R$	1.5187	1.4483	1.4333
$C_2^R$	0.4975	0.7687	0.3621
$C_3^R$	1.2500	1.4007	1.2813
$R_{adj}^2$	0.92	0.90	0.88
$p$ value	<0.05	<0.05	<0.05

where  $s(t)$  is the daily average saturation,  $s_w$  is the wilting point saturation,  $s_*$  is the saturation at incipient stomatal closure, and  $q$  is the exponent of the saturation stress equation, which is assumed equal to two [Rodríguez-Iturbe and Porporato, 2004] (Table 2).

[18] Model initial conditions were set to the incipient stomata closure saturation (Table 2), which is the point at which stress begins and we assumed the start of significant response in the vegetation to additional rainfall. We note that changing the initial condition did not significantly alter the relative order of growing season hillslope water-use efficiencies for the different vegetation-clustering strategies. The top boundary condition of the domain is a no-flow boundary and represents the top of the hillslope. The two sides of the domain are joined periodically forming a wrapped cylindrical domain. The lower boundary represents the stream channel where surface flow can exit freely out of the domain and is considered lost to the system. The system of surface and subsurface flow equations were solved separately. The system of surface flow equations was solved sequentially starting with the top of the hillslope and moving to the bottom in order to estimate the effective rainfall and coefficients for each downslope cell. We note that this ordered solve of the system variables is equivalent to a direct solution of the implicit (backward Euler) time discretization for the surface runoff. As such the method is stable even though the surface flows are faster than the Courant-Friedrichs-Lewy condition for the spatial-temporal grid [LeVeque, 1992]. Following the solution of the surface flow equations, the system of subsurface flow equations was solved with a forward Euler solution, which satisfies the Courant-Friedrichs-Lewy condition for the spatial-temporal grid given the low vertical hydraulic conductivity of the soil (Table 2).

### 2.3. Estimation of Hillslope Water Use Efficiency

[19] Using the water balance model described in section 2.2, we investigate the hillslope water use efficiency of different static spatial configurations of baregrass and baretree mosaics on a hillslope. Due to the stochastic nature of rainfall, we use Monte Carlo simulations of growing season precipitation (daily rainfall depth and rate) and average over the ensemble of growing seasons to estimate the seasonal water balance. We found that averaging twenty growing seasons and three spatial patterns was sufficient for obtaining stable means of each seasonal water balance component and seasonal water stress. The sensitivity analysis of spatial patterns and growing season realizations is presented in section 3.3.

[20] In order to more effectively search the nearly infinite parameter space of possible spatial patterns, we selected four different vegetation-clustering strategies ranging from highly organized to random given by: many aggregated clumps, many dispersed clumps, few aggregated clumps, and few dispersed clumps (Figure 2). The different spatial patterns were simulated in the following manner, which closely resembles a Neyman-Scott process. First, we selected a number of parent clustering sites,  $N_p$ , where each site is randomly located in the  $120 \times 120$  cell domain. Next, a new vegetation patch was placed from a randomly selected parent site, at a random orientation and a radial distance generated from an exponential distribution

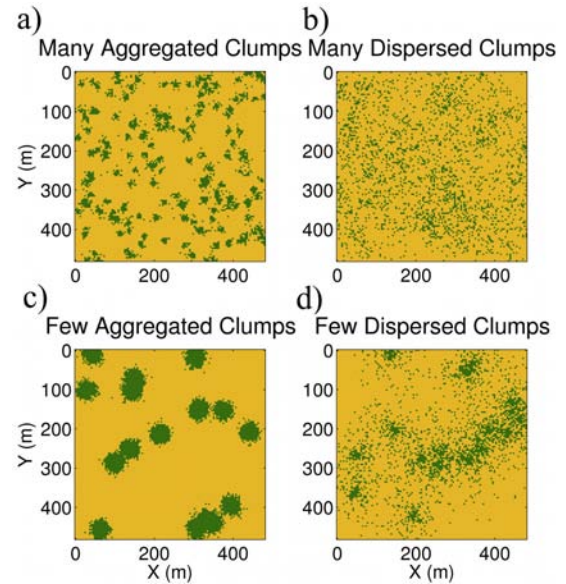


**Figure 2.** Examples of four different modeled vegetation-clustering patterns for 15% fractional cover for, (a) many aggregated clumps ( $N_p = 169$ ,  $\lambda_{pc} = 4$  m), (b) many dispersed clumps ( $N_p = 169$ ,  $\lambda_{pc} = 40$  m), (c) few aggregated clumps ( $N_p = 16$ ,  $\lambda_{pc} = 4$  m), and (d) few dispersed clumps ( $N_p = 16$ ,  $\lambda_{pc} = 40$  m).

controlled by the mean distance between parent and child sites,  $\lambda_{pc}$  (m). The process was repeated until the desired fractional cover of the domain was reached.

[21] Comparisons between each spatial pattern were evaluated with the average stress-weighted plant water use metric proposed by [Caylor et al., 2009]

$$TS = \left\langle \frac{\bar{T}}{R} (1 - \xi) \right\rangle, \quad (7)$$

where  $TS$ , is the stress-weighted plant water use metric which varies between 0 and 1,  $\frac{\bar{T}}{R}$  is the fraction of available rain water used for transpiration (assumed to be evapotranspiration from vegetated pixels) over the growing season,  $R$  is the total seasonal rainfall =  $\alpha \lambda T_{seas}$ ,  $T_{seas}$  is the length of the growing season (day), and  $\xi$  is the average daily plant water stress over the growing season. The bracket  $\langle \rangle$ , represents the spatial averaging operator of all vegetation locations in the domain, and the over bar represents the time averaging operator over the ensemble of growing seasons.

## 3. Results

### 3.1. Observational Study and Empirical Patch Water Balance

[22] The time series of daily soil moisture averaged over the top 40 cm and daily rainfall totals during the nearly 2 year observational study are presented in Figure 3. While the observational study did not explicitly consider subsurface throughflow, of the 25 rainstorms, 22 did not impact the CS616 probes at 70 cm, which indicates the majority of the soil moisture dynamics are restricted to the top 40–50 cm of the soil column. The rainstorms that did impact the deepest probes showed delayed time-to-peak soil moisture of 10–15

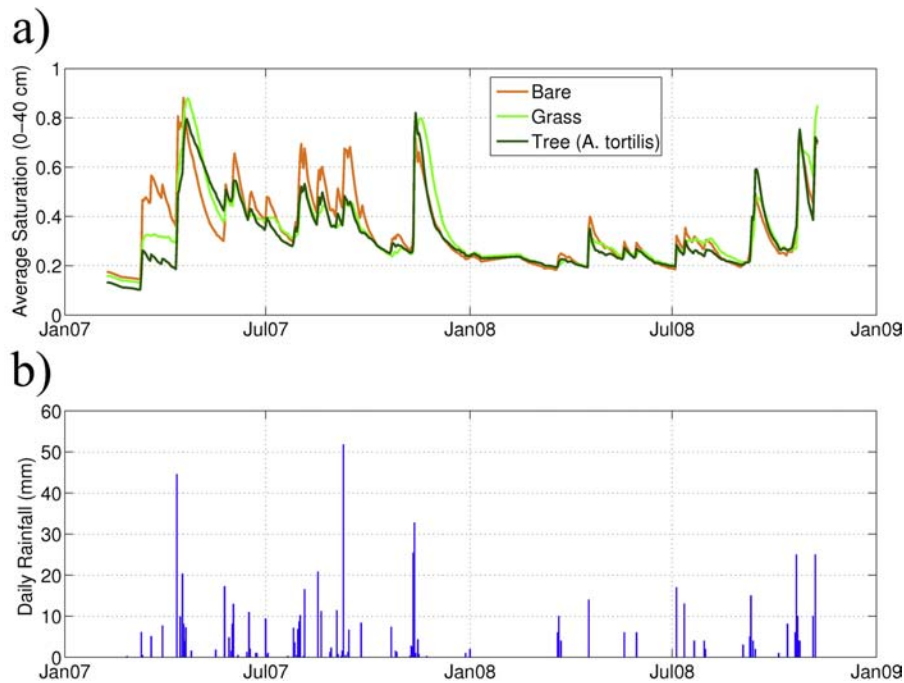


**Figure 3.** Summary of (a) CS 616 soil moisture traces averaged over the top 40 cm for bare, grass, and tree (*Acacia tortilis*) patches, and (b) daily rainfall during the observational study in central Kenya ( $0^{\circ}31'22''\text{N}$ ,  $36^{\circ}55'36''\text{E}$ ).

days compared to 1–3 days for the shallower probes. In addition, the deepest probes showed interstorm decays shaped like inverted parabolas as opposed to exponential decays at the shallower probes. The delayed time-to-peak and inverted parabolic interstorm decay shapes indicate additional sources of water other than strictly vertical infiltration from storm event water. Details on the nature of subsurface water redistribution in this area are extensively discussed in the work of Franz *et al.* [2011], but we note the influence is fairly localized around patch margins (1–10 m), and most prevalent in densely vegetated patches like *Sansevieria volkensii* where long-term vegetation dynamics are believed to be impacted by the local redistribution of subsurface water [King *et al.*, 2012].

[23] We found that the shallower probes interstorm soil moisture traces followed an exponential decay with  $R^2$  values over 0.9 for the 15 periods analyzed. Statistical analysis comparing the mean patch  $k$  values using Tukey's HSD test found statistically significant differences in the means at the 0.05 confidence level (Table 2) [Walpole *et al.*, 2002]. By comparing the relative  $k$  values we found that the highest rate of water use occurred in bare soil, followed by tree with grass, and grass. The mean daily patch water use compares well with the maximum estimated evapotranspiration for each patch (Table 2). In addition, we found that the individual  $k$  values were independent (linear correlations less than 0.05) of rain depth, rain rate, and antecedent soil moisture. We note that additional CS616 probes around the study area in *A. mellifera* and *A. etbaica* patches illustrate similar interstorm decay rates as the *A. tortilis* patch used in this study. We selected *A. tortilis* as the representative tree species for this modeling study because of the existing literature on the species and the coupled CS616 and runoff data.

[24] In contrast, we found that surface runoff was highly correlated to average daily rain rate and total rainfall, with  $R^2$  values near 0.9 for the generalized linear models summarized in equation (5) and Tables 4 and 5. By representing the surface runoff generation with an empirical relationship, we were able to construct a simplistic representation of the patch storm event water balance (Figure 4). The storm event patch water balance presented in Figure 4 illustrates the various water balance components, runoff, infiltration, leakage, and event losses, for different total rainfall, three rain rates (low, average, high), and two antecedent soil moisture conditions (dry and wet). For all cases, we found that bare soil had the greatest amount of runoff generation and the lowest vertical leakage. Runoff values for all patches increased with higher rain rates. Leakage values also greatly increased with higher antecedent soil moisture conditions. Overall, the simplistic patch water balance follows expected behavior of the represented processes and allows us to more easily construct complex spatial interactions, which are believed to drive vegetation structure in this system.

### 3.2. Model Validation

[25] As is the case with most drylands [Wilcox and Newman, 2005], the annual runoff ratio of the Upper Ewaso Ng'iro River Basin is less than 5%, where rainfall and glacial melt on Mount Kenya feed water to the rest of the basin [Franz, 2007]. Using 25 years of precipitation data and streamflow data upstream and downstream of the study area, the average annual runoff ratio is  $\sim 1\%$  [Franz, 2007]. Given the low runoff values, classic model validation with streamflow data is not totally satisfactory as 99% of the annual water balance is evapotranspiration. Currently in the

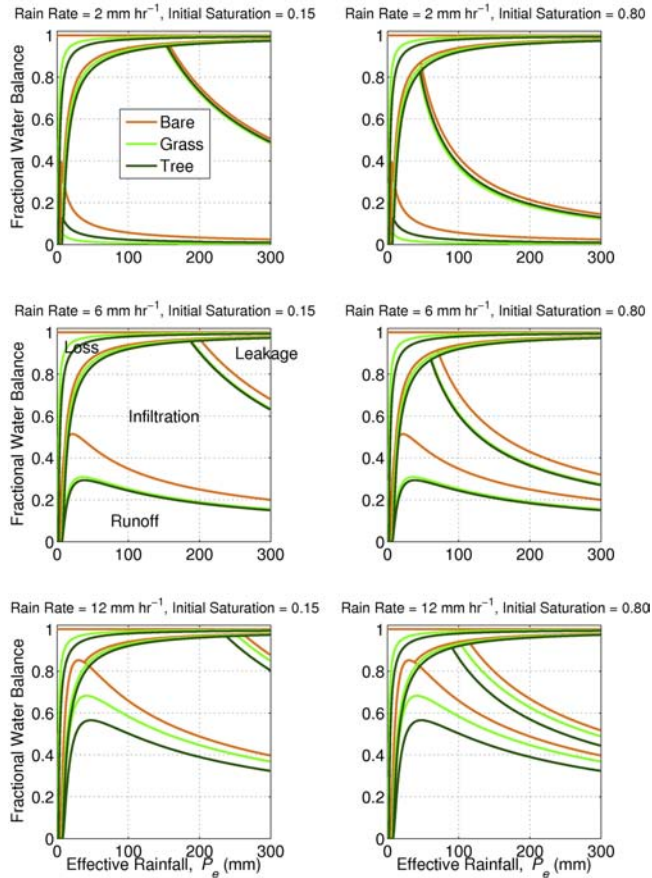


**Figure 4.** Summary of empirically derived event water balance for representative bare, grass, and tree patches. Panels summarize the event water balance components of runoff, infiltration, losses, and vertical leakage for three different rain rates (low, top panels; average, middle panels; high, bottom panels) and two different antecedent soil moisture conditions (dry, left panels; and wet, right panels).

study area, a 25 m tall eddy covariance tower and isotope techniques are being used to partition evaporation and transpiration over a wide range of temporal scales at the landscape level (K. K. Caylor, unpublished data, 2011). In addition, flumes are being installed in smaller ephemeral basins to obtain more resolved runoff data. As these datasets become available more finely resolved model calibration and validation tests would be possible.

[26] In terms on the annual water balance, the model performance is consistent with the observations. At tree densities of 20%, the annual runoff is 1%–2% with a maximum value of 5% for all simulations performed. We note that the modeled runoff is consistent at the plot scale (Table 4) where local runoff is often greater than 50% of incoming precipitation (Figure 4) and at the integrated landscape scale where streamflow data is available. In addition, the individual time series of soil moisture for each patch are recovered from the observed rainfall. The remaining annual water balance terms for the 20% tree density simulations indicate interception <0.1%, leakage ~1%, evapotranspiration from vegetated patches at 10%–25%, and bare soil evaporation at 50%–80% for all simulations performed.

### 3.3. Model Sensitivity

[27] A full sensitivity analysis of parameters for the non-spatial form of this model is performed elsewhere [Franz *et al.*, 2010]. Here we focus on the new spatial components of the model, which include the redistribution of surface water and the ability of vegetation to use water from its neighbors. In addition, we perform a sensitivity test on the most efficient vegetation patterns where we vary the mean values of the random variables controlling the stochastic rainfall process with the results presented in section 3.5.

[28] An emergent property of this dryland ecosystem and many drylands is the redistribution of surface water from Hortonian generated runoff. Instead of trying to model the physical processes explicitly, we took a complex adaptive systems approach [Harte, 2002; Levin, 1998] to generate the general behavior observed in these systems. In our simple water balance model the level of local surface flowpath convergence is controlled by the parameter,  $fr$ , which is the fraction of runoff to a downslope vegetation patch (equation (4)). Based on a few simple rules of the local neighborhood, we were able to generate a wide range of system flow convergence behavior by varying  $fr$ . An example of the different behavior is presented in Figure 5, where we simulated a large intense rain event on an initially saturated hillslope. By averaging over all the bare soil and tree patches we were able to describe the mean and variance of the hillslope surface flow convergence by the ratio of effective precipitation to direct precipitation,  $\frac{P_e}{P}$ . As  $fr$  approaches 0, the largest patch differences and highest variation in  $\frac{P_e}{P}$  is observed, with mean values nearly double between bare and tree patches. At  $fr$  values near 0.2, the mean and variance of  $\frac{P_e}{P}$  is about one third larger in bare patches compared to tree patches. As  $fr$  approaches 0.4, the difference in the mean and variance of  $\frac{P_e}{P}$  between the patches goes to 0, resulting in a neutral redistribution of surface water. At  $fr$  values greater than 0.4, tree patches begin to receive higher  $\frac{P_e}{P}$  compared to bare patches. The parameter becomes unbounded for values greater than ~0.58.

[29] In order to evaluate the efficiency of different hillslope vegetation patterns, we compared the average growing season plant water use and plant water stress (equation (7)). Given the random fluctuations in the rainfall properties, we stochastically simulated different realizations of the growing season daily precipitation from the mean values of the random variables estimated from gauge data (Table 1). As a way of approximating a stable mean of the  $TS$  metric, we performed a sensitivity analysis of  $TS$  by separately varying the number of realizations of spatial patterns (holding  $N_p$ ,  $\lambda_{pc}$ , and total fractional cover constant) and the number of growing seasons (holding  $\alpha$ ,  $\lambda$ , and  $i$  constant). The mean and standard error values of the  $TS$  metric are presented in Figure 6 for the four different vegetation-clustering patterns. The results indicate that the variation in  $TS$  is more sensitive (greater than 1 order of magnitude) to stochastic variation in growing season rainfall patterns compared to variation in generated spatial patterns. In order to reduce computational costs, we assume that averaging twenty growing seasons for three realizations of each vegetation-clustering pattern provides a stable mean of the  $TS$  metric, as further increases in the number

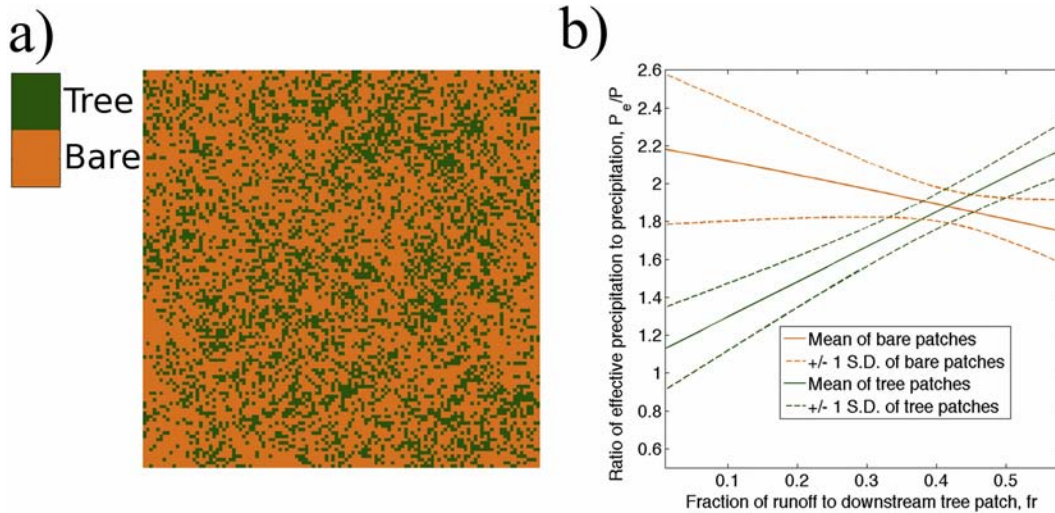


**Figure 5.** Example of (a) baretree model domain and (b) sensitivity of surface flow convergence parameter,  $f_r$ , to the mean and variability of the ratio of effective rainfall to local precipitation averaged over all bare and tree patches in the domain.

of growing season sample sizes only moderately reduced the standard error.

**3.4. Spatial Clustering of Vegetation Patterns**

[30] Using the high-resolution imagery available for the study site, we identified the natural organization of vegetation patterns by analyzing the vegetation contiguous cluster size distribution following [Scanlon *et al.*, 2007]. After classification of the image into bare, grass, and tree pixels (Guan *et al.*, 2012, in preparation) (Figure 1c), we defined contiguous clusters as vegetation pixels that were connected through any shared edge (four immediate neighbors, von Neumann neighborhood, no diagonals) in a 400 m × 400 m area. We further partitioned the 400 m × 400 m areas by different total fractional vegetation cover and by areas dominated by grass or tree pixels. The cumulative distribution functions (cdf) of grass and tree cluster sizes for 10%, 20%, 30%, and 40% fractional covers are presented in Figures 7a–7d. The empirical cdf’s and 95%

confidence intervals were created from eight to twelve 400 m × 400 m images in each of the different classes. All cdf’s more closely fit an exponential model compared to a power law distribution with  $R^2$  values in excess of 0.99. With increasing fractional cover, the median cluster size increased from ~300 m<sup>2</sup> at 10% to ~500 m<sup>2</sup> at 40%. In addition, the upper tail of the distribution shifted by over an order of magnitude for increasing fractional cover. Figure 7a indicates that the grass and tree cdf’s were nearly identical at 10% fractional cover. Figures 7b and 7c illustrates that at 20% and 30% fractional cover the tree cdf shifted to relatively larger median cluster sizes compared to the grass cdf. As shown in Figure 7d, at 40% fractional cover, the grass and tree cdf’s appear to be converging to a similar distribution.

[31] In order to help interpret the observed vegetation patterns we computed the patch size cdf’s of one realization of the different modeled vegetation-clustering strategies at each fractional cover (Figures 7e–7h). The range of the

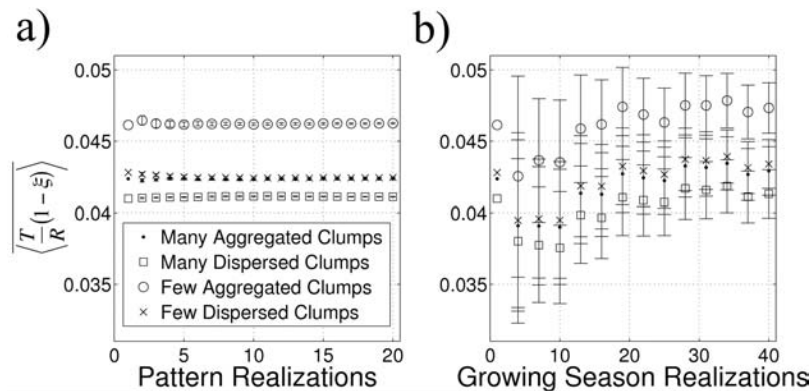


**Figure 6.** Sensitivity of  $TS$  metric to (a) the number of pattern realizations averaged and (b) the number of growing season realizations averaged, for four different patterns of vegetation. Note: error bars in figure denote  $\pm 1$  standard error.

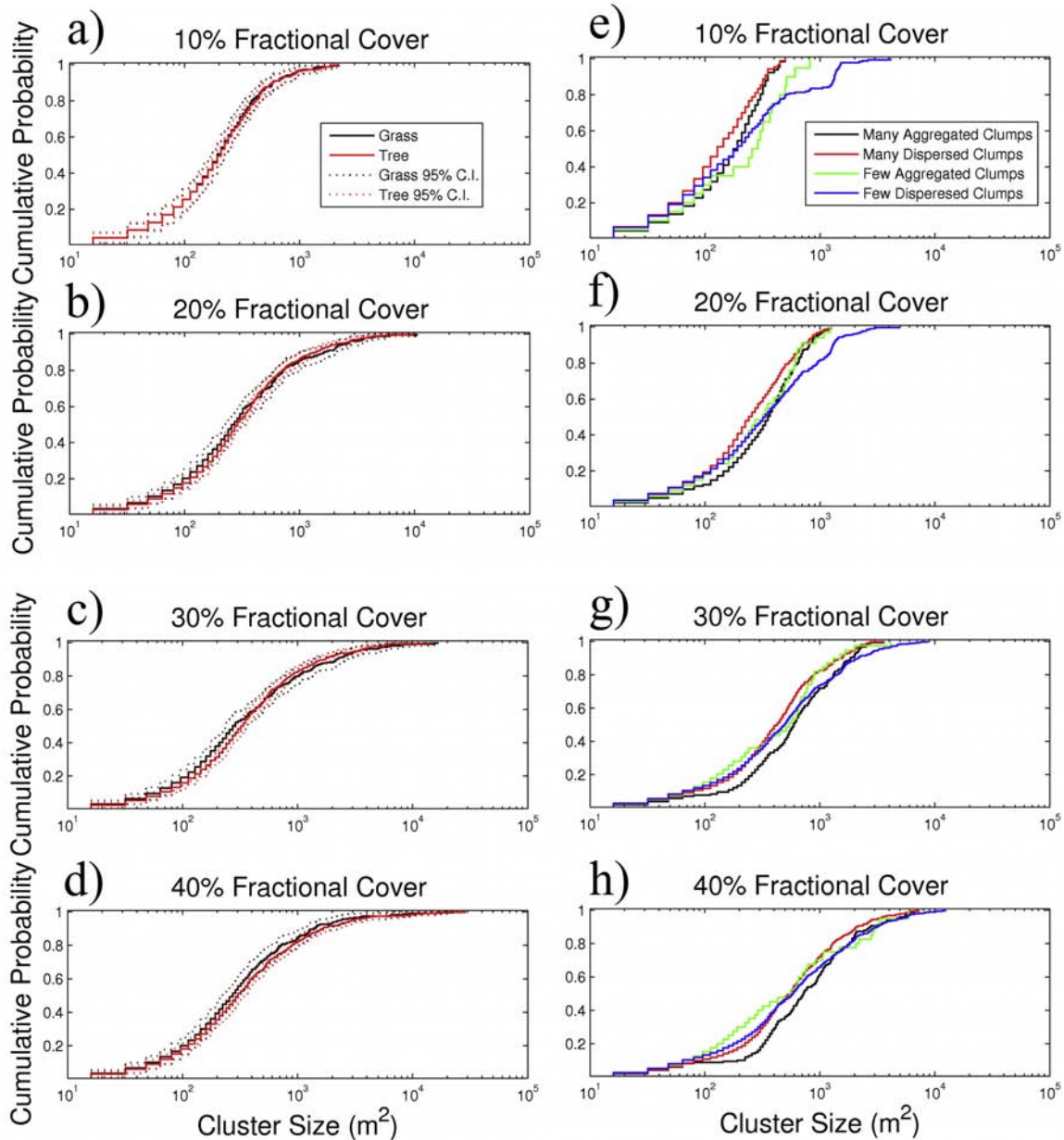


**Figure 7.** Cumulative distributions and 95% confidence intervals of observed vegetation cluster sizes for different fractional covers, (a) 10%, (b) 20%, (c) 30%, and (d) 40%, of grass and tree dominated areas. Between 8 and 12, 400 m  $\times$  400 m sample areas from the satellite imagery were used to estimate the different cumulative distributions and confidence intervals. Cumulative distributions of vegetation cluster sizes for different fractional covers, (e) 10%, (f) 20%, (g) 30%, and (h) 40%, for one realization of four different modeled vegetation-clustering patterns.

four different modeled vegetation-clustering strategies provided reasonable comparisons with the observed patterns. As with the observed patterns, the median cluster size increased with increasing fractional cover. Also with increasing fractional cover, the strategy of many aggregated clumps produced larger cluster sizes compared to the other three strategies. The largest discrepancy between the empirical and modeled cdf's is that the modeled patterns are not able to fully capture the upper tail behavior at frac-

tional covers of 30% and 40%. The reason for this discrepancy is that 5%–10% residual grass or tree cover existed in the observational data for the tree or grass dominated areas (Figure 1c), which may skew the observed cluster size distribution. Most importantly, the cdf's (Figures 7e–7h) and example clustering strategies (Figure 2) illustrate that the four different modeled vegetation-clustering strategies provide a pragmatic approach to exploring the nearly infinite parameter space of possible spatial patterns.

### 3.5. Modeled Organization of Hillslope Vegetation Patterns

[32] Using the  $TS$  metric as a way to select the most efficient hillslope vegetation spatial pattern, we present the most efficient patterns at 20% fractional cover for increasing  $fr$  values and two different  $RCR$  parameter values (Figure 8). By breaking down the  $TS$  metric (Figures 8a and 8b), we can evaluate the relative changes in seasonal plant water use  $\langle \frac{T}{R} \rangle$  and water stress avoidance  $\langle (1 - \xi) \rangle$  individually. Figures 8a and 8b illustrates how each component of the  $TS$  metric changed for each vegetation-clustering strategy as a function of  $fr$  and  $RCR$ . At an  $RCR = 1$ , we found that  $\langle \frac{T}{R} \rangle$  increased with increasing  $fr$  values with the maximum curvature at high  $fr$  values. The different vegetation-clustering strategies increased at different rates, leading to crossover of the strategy with the largest relative magnitude of  $\langle \frac{T}{R} \rangle$ . At an  $RCR = 3$ , again we found that  $\langle \frac{T}{R} \rangle$  increased with increasing  $fr$ , but the relative magnitude of  $\langle \frac{T}{R} \rangle$  shifted upward compared to an  $RCR = 1$  and the slope became comparatively more nonlinear. The magnitude of the shift in  $\langle \frac{T}{R} \rangle$  was not equal between the four strategies, leading to the many dispersed clumps strategy having the largest  $\langle \frac{T}{R} \rangle$  for all  $fr$  values. In comparison, we found that the different

vegetation-clustering strategies followed the same general trend in  $\langle (1 - \xi) \rangle$  for increasing  $fr$  and  $RCR = 1$  and  $RCR = 3$ . At low  $fr$  values the strategy of a few aggregated clumps had the highest  $\langle (1 - \xi) \rangle$  value and at around  $fr = 0.25$ – $0.30$  the strategy with the highest  $\langle (1 - \xi) \rangle$  value switched to many dispersed clumps. The consequences to the  $TS$  metric are presented in Figure 8c, where we see the switch in the optimal strategy from a few aggregated clumps to many dispersed clumps with increasing  $fr$ . At  $fr = 0.15$ – $0.25$ , we see the four strategies converging to the same mean  $TS$  metric value. Depending on the realization of the spatial pattern and climatic inputs, any of the four strategies may result in the highest mean  $TS$  metric value.

[33] In addition to varying the local surface convergence and root to canopy ratios, we performed simulations that varied the mean values of the random variables that control the stochastic rainfall process (Figure 9 and Table 6). By varying mean storm depth ( $\alpha$ ) and storm arrival rate ( $\lambda$ ) we are able to change the mean growing season precipitation ( $\mu = \alpha\lambda T_{seas}$ ) while holding the variance of growing season precipitation constant ( $\sigma^2 = 2\alpha^2\lambda T_{seas}$ ) and vice versa. The results in Figure 9 illustrate that changes in the total rainfall, rainfall variability, and storm intensity do not

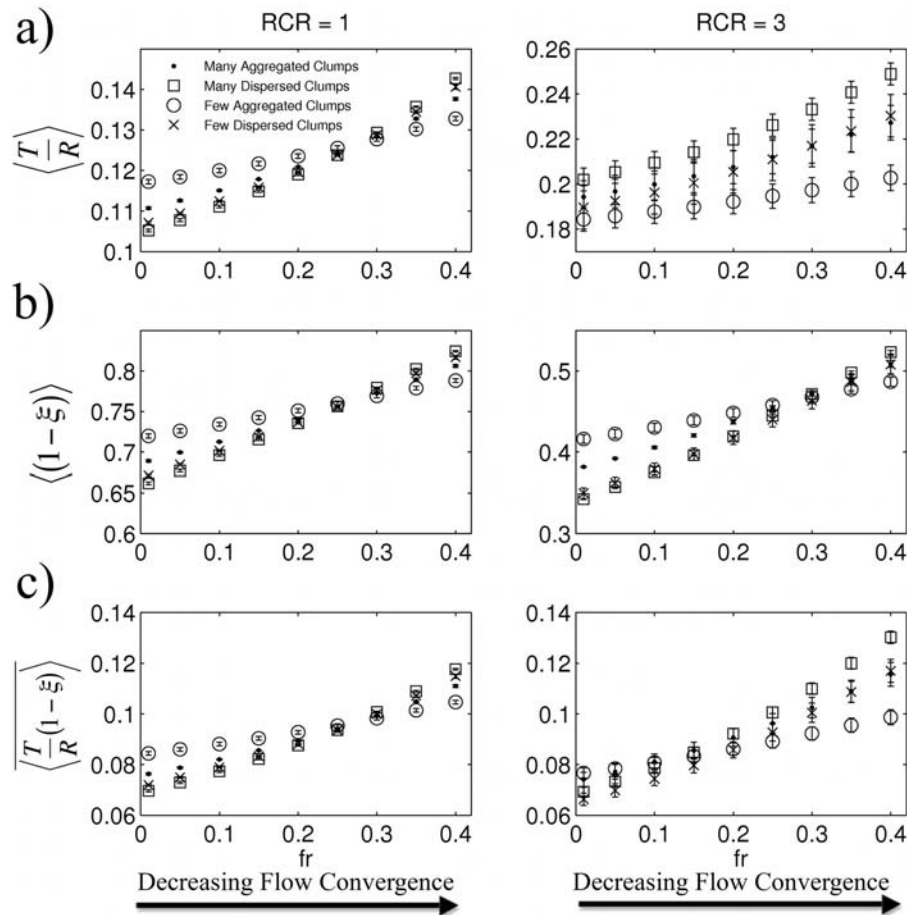


**Figure 8.** Summary of (a) average growing season plant water use  $\langle \frac{T}{R} \rangle$  (b) average growing season stress avoidance  $\langle (1 - \xi) \rangle$ , and (c)  $TS$  hillslope efficiency metric for different surface flow convergence parameter values  $fr$ , and two different root to canopy radius parameter values  $RCR$ . Note error bars are  $\pm 1$  standard deviation of each pattern realization, fractional cover was held constant at 20%, and the change in scale for they axis in Figures 8a and 8b for each  $RCR$  value.

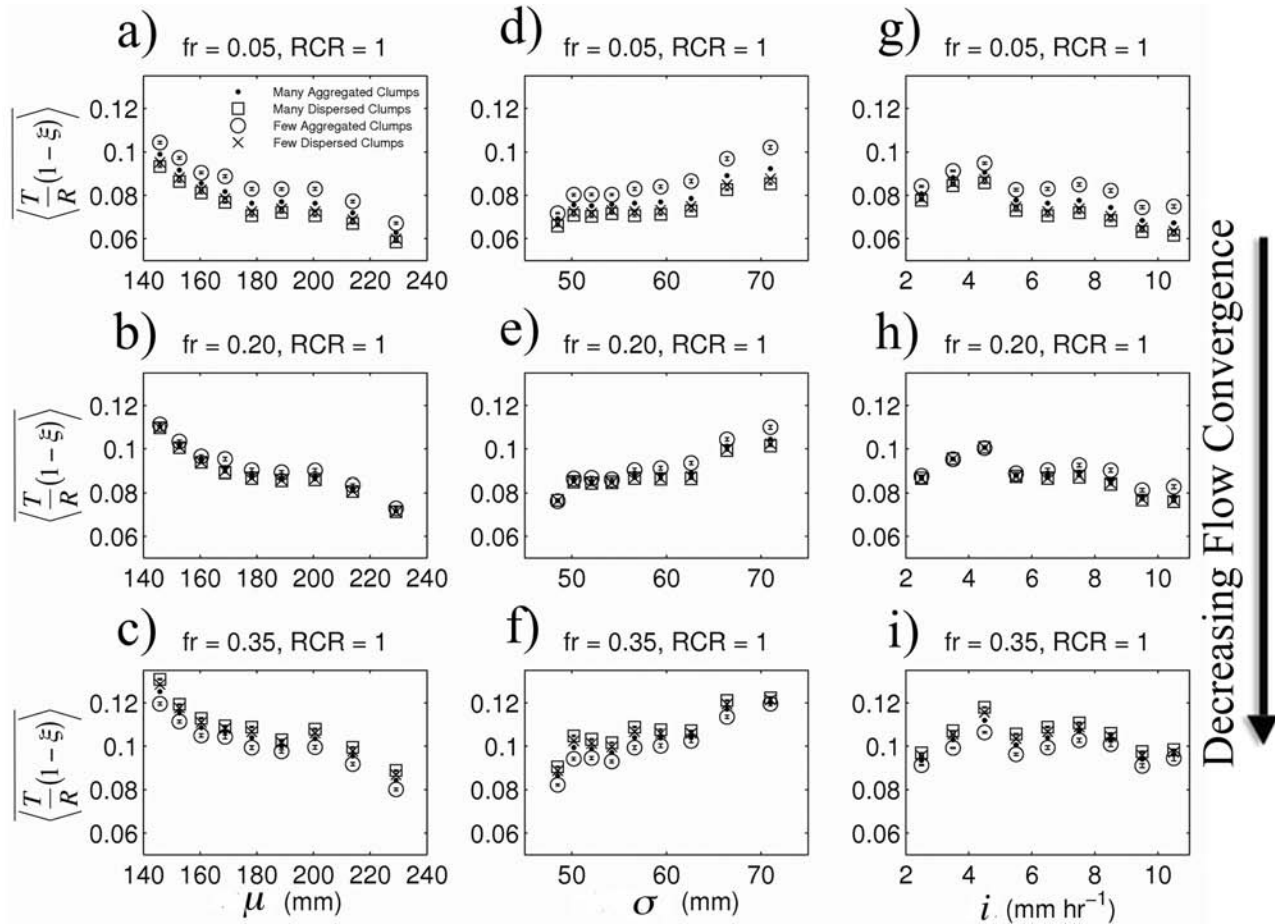


**Figure 9.** Summary of *TS* hillslope efficiency metric for three different surface flow convergence parameter values,  $fr = 0.05, 0.20, 0.35$ , and root to canopy radius,  $RCR = 1$ , (a–c) by varying total growing season precipitation,  $\mu$ , while holding the standard deviation of growing season precipitation,  $\sigma$ , and mean rainfall intensity,  $i$ , constant, (d–f) varying  $\sigma$  while holding  $\mu$  and  $i$  constant, and (g–i) varying  $i$  while holding  $\mu$  and  $\sigma$  constant. Note error bars are  $\pm 1$  standard deviation of each pattern realization and fractional cover was held constant at 20% and specific scenarios can be found in Table 6.

affect the relative order of most efficient spatial patterns for a given  $fr$  and  $RCR$  value. Interestingly, it is only changes in the surface flow convergence parameter  $fr$ , that result in changes in the most efficient vegetation-clustering strategy indicating that the localized model parameter controls the order of the most efficient vegetation pattern as opposed to the global rainfall parameters.

## 4. Discussion

### 4.1. Comparison of Observed and Modeled Vegetation Patterns

[34] The timescale for trees to reach maturity makes experimental studies impractical, leaving only a single realization of the natural process to observe and interpret. An alternative strategy is to recreate the evolution of the vegetation patterns [Jeltsch *et al.*, 1996; van Wijk and Rodriguez-Iturbe, 2002]. Depending on the strength of the nonlinearities, chaotic behavior may arise requiring a complete time history to reconstruct system dynamics [Boyce and DiPrima, 2001]. Adding to the complexity,

the random fluctuations of rainfall in dryland ecosystems require a stochastic treatment of the process [Katul *et al.*, 2007].

[35] As a first step toward understanding the full dynamical system of vegetation patterns on hillslopes, we investigated the most efficient steady state patterns derived from a simple water balance model and compared them with a snapshot of the ecosystem from high-resolution imagery. Analysis of the observed cluster size distribution indicated all distributions more closely fit an exponential compared to a power law distribution. The high-resolution imagery revealed that at fractional covers of 10% and 40%, trees and grasses have a similar observed cluster size distribution. At low fractional cover and given the likelihood of longer connected bare soil flowpaths, the model results suggest that the driving mechanism controlling the vegetation pattern is the strategy that most effectively conserves system water loss. As the fractional cover approaches the percolation threshold near 0.59 for a von Neumann neighborhood [Stauffer and Aharony, 1985], the importance of connected pathways diminishes. Here, the influence of

**Table 6.** Summary of Input Parameters for Rainfall Sensitivity Analysis, see Figure 9 for Results

Scenario	Mean Daily Storm Depth, $\alpha$ (mm)	Mean Storm Arrival Rate, $\lambda$ ( $\text{day}^{-1}$ )	Average Rainfall Rate, $i$ ( $\text{mm h}^{-1}$ )	Total Rainfall per Growing Season, $\mu$ (mm)	SD of Rainfall per Growing Season, $\sigma$ (mm)
vary $\mu$	7.00	0.364	6.5	229.1	56.6
vary $\mu$	7.50	0.317	6.5	213.8	56.6
vary $\mu$	8.00	0.278	6.5	200.5	56.6
vary $\mu$	8.50	0.247	6.5	188.7	56.6
vary $\mu$	9.00	0.220	6.5	178.2	56.6
vary $\mu$	9.50	0.198	6.5	168.8	56.6
vary $\mu$	10.00	0.178	6.5	160.4	56.6
vary $\mu$	10.50	0.162	6.5	152.7	56.6
vary $\mu$	11.00	0.147	6.5	145.8	56.6
vary $\sigma$	14.14	0.140	6.5	178.2	71.0
vary $\sigma$	12.38	0.160	6.5	178.2	66.4
vary $\sigma$	11.00	0.180	6.5	178.2	62.6
vary $\sigma$	9.90	0.200	6.5	178.2	59.4
vary $\sigma$	9.00	0.220	6.5	178.2	56.6
vary $\sigma$	8.25	0.240	6.5	178.2	54.2
vary $\sigma$	7.62	0.260	6.5	178.2	52.1
vary $\sigma$	7.07	0.280	6.5	178.2	50.2
vary $\sigma$	6.60	0.300	6.5	178.2	48.5
vary $i$	9.00	0.220	2.5	178.2	56.6
vary $i$	9.00	0.220	3.5	178.2	56.6
vary $i$	9.00	0.220	4.5	178.2	56.6
vary $i$	9.00	0.220	5.5	178.2	56.6
vary $i$	9.00	0.220	6.5	178.2	56.6
vary $i$	9.00	0.220	7.5	178.2	56.6
vary $i$	9.00	0.220	8.5	178.2	56.6
vary $i$	9.00	0.220	9.5	178.2	56.6
vary $i$	9.00	0.220	10.5	178.2	56.6

plant-plant competition seems to drive system behavior, which is manifested in the plant water stress component. With increasing fractional cover, vegetation is more likely to be located next to one another, where the distance of overlapping roots influences the spread of vegetation. Observations at fractional covers of 20% and 30% revealed that trees and grasses have different cluster size distributions where tree clusters tend to form larger clusters at the same probability level. It is at these intermediate fractional covers where the spatial patterns are most sensitive to mitigating resource use and scarcity.

[36] We present model efficiency analyses at the intermediate fractional cover of 0.2 in Figures 8 and 9, which illustrates the most efficient clumping strategy by varying the surface flow convergence parameter,  $fr$ , and the root to canopy ratio parameter,  $RCR$ . Our model results show a switch in the most efficient strategy, where at high  $fr$  values (neutral redistribution of surface flow to bare and vegetated patches) the strategies of dispersed clusters have the two highest  $TS$  metric values. In contrast, at low  $fr$  values (convergent flow in connected bare soil patches) we find that the strategy of aggregated clumps have the two highest  $TS$  metric values. The effects of an increasing  $RCR$  value result in higher relative plant water use (Figure 8a) and lower stress avoidance values (Figure 8b). Overall, the combined effects of increased resource use and decreased stress avoidance does not greatly alter the relative order of efficiency of clumping strategies (Figure 8c), but it does slightly shift the location of the crossover point from  $fr = 0.25$  at an  $RCR = 1$  to an  $fr = 0.15$  at an  $RCR = 3$ , indicating the effects of different rooting strategies in comparing various static spatial patterns.

#### 4.2. Observed Changes in Facilitation and Competition in Dryland Ecosystems

[37] Using a simplistic water balance model representative of bare soil, grass, and tree patches of a central Kenya dryland, we are able to demonstrate various most efficient static spatial patterns which are consistent with high-resolution satellite imagery of the study area. The model is able to demonstrate a range of most efficient static vegetation patterns from highly organized to random by varying the  $fr$  and  $RCR$  parameters. Depending on the value of these parameters, the length scales of competition and facilitation change to form different patterns [Barbier *et al.*, 2008; Borgogno *et al.*, 2009; Manor and Shnerb, 2008]. Observations from satellite imagery of this dryland ecosystem indicate vegetation-clustering patterns that follow exponential distributions instead of power laws. Given the recent history (4–5 decades) of intense grazing in this ecosystem [King *et al.*, 2012], our observations are consistent with recent predictions of exponential distributions prevalent in degraded landscapes [Kefi *et al.*, 2007; Scanlon *et al.*, 2007]. However, given the time lag for trees to reach maturity it is unclear whether the distribution of clusters has been affected by grazing or whether the patterns have ever followed power law distributions. Without an extensive historical record (many decades), it is not possible to reconstruct the observed changes in woody canopy cluster distributions.

[38] As an alternative, we believe our modeling results support a framework to understand signs of degradation in this ecosystem. The current situation of intense grazing practices in central Kenya has led to the recent transition

from a tree-grass savanna to a baretree matrix. The expansion of bare soil areas has led to an increase in Hortonian runoff and subsequent development of rills and gullies affecting the convergence of surface flow paths. The model results presented in Figure 8 indicate the transition to a few aggregated cluster strategy as most efficient as  $fr$  values approach zero. Future studies in these types of systems, in particular the recent expansion of *Sansevieria volkensii* in central Kenya [King *et al.*, 2012], may be able to use this modeling framework as a tool to test hypotheses of new pattern formation. The observations and modeling framework provide support that symmetry-breaking instabilities [Borgogno *et al.*, 2009] drive vegetation patterning in dryland ecosystems.

#### 4.3. Comparison of Hillslope Efficiency Metrics

[39] While support exists for using the resource trade-off hypothesis in dryland ecosystems [Caylor *et al.*, 2009], we further test this hypothesis by comparing the most efficient vegetation-clustering patterns with two other possible hillslope efficiency metrics.

[40] The first alternative candidate we investigated is given by minimizing the sum of hillslope water losses  $HL$ ,

$$HL = 1 - \left( \frac{L+Q}{R} \right), \quad (8)$$

where  $L$  is the sum of leakage out of the rooting zone for all patches over the growing season,  $Q$  is the sum of runoff

out of the domain over the growing season,  $R$  is the total seasonal rainfall =  $\alpha\lambda T_{seas}$ ,  $T_{seas}$  is the length of the growing season, and the over bar represents the time averaging operator over the ensemble of growing seasons. The second alternative metric we investigated is the directional leakiness index,  $DLI$ , which was developed to assess potential soil loss on hillslopes (minimization of the distribution of flowpath lengths) [Ludwig *et al.*, 2002]. The advantage of  $DLI$  is its estimation of landscape leakiness with readily available remotely sensed data products.

[41] The comparisons of the different metrics are presented in Figure 10 for a range of  $fr$  values. We find that the  $HL$  and  $1-DLI$  metrics are consistent with the rankings of different vegetation clustering strategies. For all values of  $fr$ ,  $HL$  and  $1-DLI$  (metric not a function of  $fr$ ) predict the many dispersed clumps strategy to be the most efficient and the few aggregated clumps strategy to be the least efficient. Comparison of all three metrics agree when  $fr > 0.25$ , when the redistribution of surface water is neutral between bare and vegetated patches. However, at  $fr < 0.25$  the metrics give opposite predictions in the most efficient clustering strategy. Neglecting the differences in the  $1-DLI$  metric because it is independent of  $fr$ , Figures 8 and 10 illustrate that with smaller hillslope losses, the few aggregated clump strategy is able to capture more water than the other strategies at low  $fr$  values, which leads it to have higher water use and lower stress.

[42] Because the model only looks at the three downslope neighbors, vegetation patches with three or more

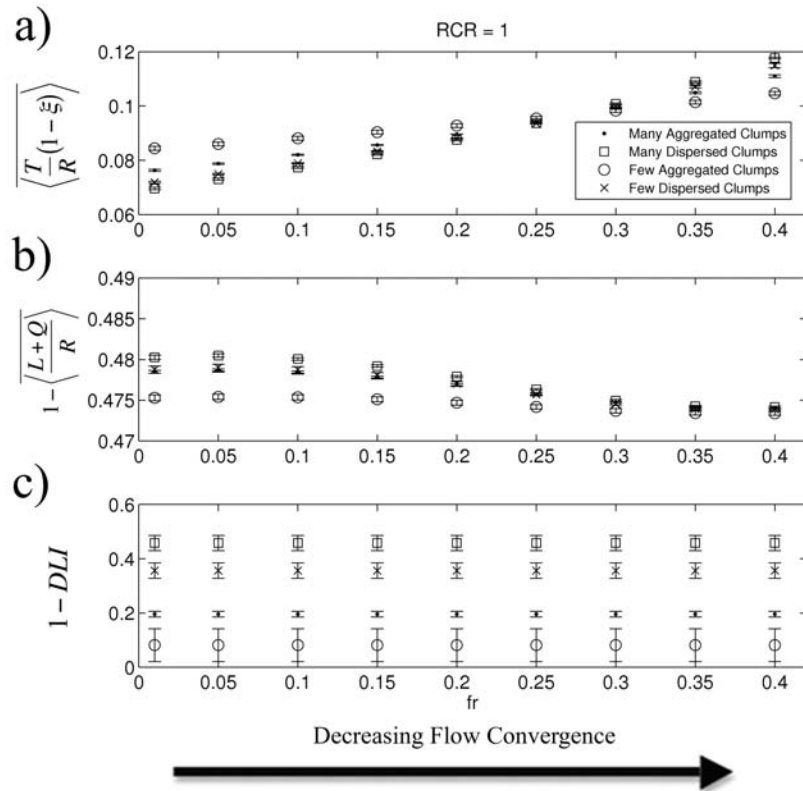


**Figure 10.** Summary of (a)  $TS$ , (b)  $HL$ , and (c)  $1-DLI$  hillslope efficiency metrics for different surface flow convergence parameter values  $fr$  and an  $RCR = 1$ . Note error bars are  $\pm 1$  standard deviation of the different baretree pattern realizations.

pixels will be able to effectively access the water in an upslope flowpath. This is similar to the mechanism responsible for cellular automata models that predict the migrating tigerbush bands at low slopes [Dunkerley, 1997; Lefever and Lejeune, 1997]. Because the slopes at this site are more severe, we assumed the redistribution of surface water is limited to just the three downslope neighbors. Preliminary dynamic vegetation results with the proposed ecohydrological modeling framework suggest migrating vertically oriented ellipses to be one possible nontrivial stable solution.

[43] Given the availability of remote sensing products, simple metrics like *DLI* [Ludwig et al., 2002, 2006, 2007], seem to provide a reasonable assessment of relative hillslope water losses for different vegetation spatial patterns. However, the differences in the *HL* and *l-DLI* metrics with the *TS* metric at low *fr* values, indicates that maximization of only the limiting resource is not enough to accurately predict system behavior [Kerkhoff et al., 2004]. The moderating effects of plant water stress play a vital role in this dryland ecosystem.

#### 4.4. Limitations of This Study

[44] While the simple water balance model was able to demonstrate the efficiency of a range of static distribution patterns on hillslopes, the model is still a preliminary step in understanding the principles that govern dryland vegetation patterns. The main limitation of the current work is the static treatment of vegetation. The justification is that an important first step in studying coupled nonlinear equations is to establish the character of the critical points in the system. The current work identifies two stable critical points that are represented by the many dispersed clumps vegetation-clustering strategy at high *fr* values and the few aggregated clumps strategy at low *fr* values. The model results suggest a switch in these two strategies at *fr* values near 0.2, where all four strategies collapse to the same *TS* value. Despite the limitations of treating vegetation statically, identification of these two stable strategies and transition point will greatly facilitate in understanding dynamic vegetation patterns.

[45] Another limitation is that the empirical water balance was developed from a single set of experiments. While the simple water balance follows the expected behavior of the modeled processes, the role of changes in slope on runoff generation should be included [Quinn et al., 1991]. In addition, the functional dependence of the *fr* parameter with slope, rain depth, rain intensity, vegetation type and sediment transport will likely be important. For computational efficiency, the *RCR* metric was limited to a maximum value of three, however the extent of the roots may extend well beyond the canopy with values approaching ten in other drylands [Lejeune et al., 2004]. In addition, *RCR* is likely a function of hillslope position, as studies have shown transpiration rates to be a function of hillslope position [Tromp-van Meerveld and McDonnell, 2006]. An interesting next step of this modeling framework would be to allow *RCR* to vary as a function of position and assess the impacts to the annual water balance and derived optimal static patterns through the *TS* metric. Finally, we found that ~90% of the rainfall dynamics were limited to the top 40 cm of the soil column. However,

widespread bioturbation [Darlington, 1997] and increases in densely populated species in this ecosystem cause preferential vertical infiltration points [Franz et al., 2011], leading to redistribution of subsurface water on the timescales of many days to weeks. While the subsurface redistribution is fairly localized [Franz et al., 2011], the impacts on the surrounding vegetation communities in this ecosystem have been profound, as subsurface redistribution is the likely mechanism responsible for the rapid proliferation of an undesirable native succulent [King et al., 2012]. In addition, studies from other drylands have found hydraulic lift and the vertical redistribution of water via root systems to be a critical source of water and buffer against plant stress in times of extended drought [Otieno et al., 2005; Scott et al., 2008; Williams and Albertson, 2004]. We note that our analysis did not include water use from sources deeper than 40 cm and this may be a source of bias in the results. The full influence of subsurface flow processes and the role of deeper sources of water on the organization of dryland vegetation remains an open and challenging research topic.

#### 5. Conclusions

[46] Given the direct coupling of pastoralist societies and the structure of dryland vegetation, understanding the processes that govern the distribution of vegetation is of critical importance. In this work we develop a spatially explicit daily ecohydrologic model that investigates the spatial structure of vegetation on hillslopes. Combining the simple water balance model with the resource trade-off hypothesis governing dryland vegetation patterns, we are able to demonstrate a range of most efficient static vegetation clustering distribution patterns by varying the length scales of the parameters that control facilitation and competition. The work provides an example from the drylands of central Kenya where symmetry-breaking instabilities govern the observed vegetation patterns. In addition, the model provides a framework to study the recent proliferation of the undesirable succulent *S. volkensii*, which may have devastating consequences on the communal grazing lands of central Kenya. With the continued development of such tools, quantitative and predictive information can be given to land managers to help reverse the cycle of degradation and restore the system back to its historic productive tree-grass state.

[47] **Acknowledgments.** The authors would like to thank the Mpala Research Center and Koiya Group Ranch for onsite support in Kenya. K.K. Caylor and T.E. Franz would like to thank NSF OISE-0854708, NSF CAREER award to K. Caylor EAR 847,368, and Princeton University funding sources including: Grand Challenges, Walbridge Fellowship, and Technology for Developing Regions Fellowship for their financial support. The authors would also like to thank Kaiyu Guan and Alex Lester for their contributions. The authors would also like to thank three anonymous reviewers for their helpful comments.

#### References

- Barbier, N., P. Couteron, J. Lejoly, V. Deblauwe, and O. Lejeune (2006), Self-organized vegetation patterning as a fingerprint of climate and human impact on semi-arid ecosystems, *J. Ecol.*, 94(3), 537–547, doi:10.1111/j.1365-2745.2006.01126.x.
- Barbier, N., P. Couteron, R. Lefever, V. Deblauwe, and O. Lejeune (2008), Spatial decoupling of facilitation and competition at the origin of gapped vegetation patterns, *Ecology*, 89(6), 1521–1531.

- Borgogno, F., P. D'Odorico, F. Laio, and L. Ridolfi (2009), Mathematical models of vegetation pattern formation in ecohydrology, *Rev. Geophys.*, 47, RG1005, doi:10.1029/2007RG000256.
- Boyce, W. E., and R. C. DiPrima (2001), *Elementary Differential Equations and Boundary Value Problems*, 7th ed., John Wiley, New York.
- Caylor, K. K., T. M. Scanlon, and I. Rodriguez-Iturbe (2009), Ecohydrological optimization of pattern and processes in water-limited ecosystems: A trade-off-based hypothesis, *Water Resour. Res.* 45, W08407, doi:10.1029/2008WR007230.
- Clapp, R. B., and G. M. Hornberger (1978), Empirical equations for some soil hydraulic-properties, *Water Resour. Res.*, 14(4), 601–604.
- Darlington, J. (1997), Comparison of nest structure and caste parameters of sympatric species of *Odontotermes* (Termitidae, Macrotermitinae) in Kenya, *Insectes Soc.*, 44(4), 393–408.
- Dingman, L. S. (2002), *Physical Hydrology*, 2nd ed., 646 pp., Prentice-Hall, Upper Saddle River, N. J.
- D'Odorico, P., F. Laio, and L. Ridolfi (2006), Vegetation patterns induced by random climate fluctuations, *Geophys. Res. Lett.* 33(19), L19404, doi:10.1029/2006GL027499.
- Dunkerley, D. L. (1997), Banded vegetation: Development under uniform rainfall from a simple cellular automaton model, *Plant Ecol.*, 129(2), 103–111.
- Eagleson, P. S. (1982), Ecological optimality in water-limited natural soil-vegetation systems. 1. Theory and hypothesis, *Water Resour. Res.*, 18(2), 325–340.
- Franz, T. (2007), Ecohydrology of the Upper Ewaso River Basin, Kenya, Msc thesis, 154 pp., Princeton Univ., Princeton, N. J.
- Franz, T. E., K. K. Caylor, J. M. Nordbotten, R. I. Rodriguez-Iturbe, and M. A. Celia (2010), An ecohydrological approach to predicting regional woody species distribution patterns in dryland ecosystems, *Adv. Water Resour.*, 33, 215–230, doi:10.1016/j.advwatres.2009.12.003.
- Franz, T., E. King, K. K. Caylor, and D. Robinson (2011), Coupling vegetation organization patterns to soil resource heterogeneity in a Central Kenyan dryland using geophysical imagery, *Water Resour. Res.*, 47, W07531, doi:10.1029/2010WR010127.
- Fratkin, E., and R. Mearns (2003), Sustainability and pastoral livelihoods: Lessons from East African Maasai and Mongolia, *Hum. Org.*, 62(2), 112–122.
- Furman, A. (2008), Modeling coupled surface-subsurface flow processes: A review, *Vadose Z. J.*, 7(2), 741–756, doi:10.2136/vzj2007.0065.
- Green, W. H., and G. A. Ampt (1911), Studies on soil physics Part I—The flow of air and water through soils, *J. Agric. Sci.*, 4, 1–24.
- Harte, J. (2002), Toward a synthesis of the Newtonian and Darwinian worldviews, *Phys. Today*, 55(10), 29–34.
- Hwang, T., L. Band, and T. C. Hales (2009), Ecosystem processes at the watershed scale: Extending optimality theory from plot to catchment, *Water Resour. Res.*, 45, W11425, doi:10.1029/2009WR007775.
- Isham, V., D. R. Cox, I. Rodriguez-Iturbe, A. Porporato, and S. Manfreda (2005), Representation of space-time variability of soil moisture, *Proc. R. Soc. A* 461(2064), 4035–4055, doi:10.1098/rspa.2005.1568.
- Istanbulluoglu, E., and R. L. Bras (2005), Vegetation-modulated landscape evolution: Effects of vegetation on landscape processes, drainage density, and topography, *J. Geophys. Res.*, 110, F02012, doi:10.1029/2004JF000249.
- Istanbulluoglu, E., and R. L. Bras (2006), On the dynamics of soil moisture, vegetation, and erosion: Implications of climate variability and change, *Water Resour. Res.*, 42, W06418, doi:10.1029/2005WR004113.
- Ivanov, V. Y., R. L. Bras, and E. R. Vivoni (2008), Vegetation-hydrology dynamics in complex terrain of semiarid areas: 1. A mechanistic approach to modeling dynamic feedbacks, *Water Resour. Res.*, 44, W03429, doi:10.1029/2006WR005588.
- Jeltsch, F., S. J. Milton, W. R. J. Dean, and N. VanRooyen (1996), Tree spacing and coexistence in semiarid savannas, *J. Ecol.*, 84(4), 583–595.
- Katul, G., A. Porporato, and R. Oren (2007), Stochastic dynamics of plant-water interactions, *Ann. Rev. Ecol. Evol. Syst.*, 38, 767–791, doi:10.1146/annurev.ecolsys.38.091206.095748.
- Kefi, S., M. Rietkerk, C. L. Alados, Y. Pueyo, V. P. Papanastasis, A. ElAich, and P. C. de Ruiter (2007), Spatial vegetation patterns and imminent desertification in Mediterranean arid ecosystems, *Nature*, 449(7159), 213–215, doi:10.1038/nature06111.
- Kelleners, T. J., M. S. Seyfried, J. M. Blonquist, J. Bilskie, and D. G. Chandler (2005), Improved interpretation of water content reflectometer measurements in soils, *Soil Sci. Soc. Am. J.*, 69(6), 1684–1690.
- Kerkhoff, A. J., S. N. Martens, and B. T. Milne (2004), An ecological evaluation of Eagleson's optimality hypotheses, *Funct. Ecol.*, 18(3), 404–413.
- King, E. G., T. E. Franz, and K. K. Caylor (2012), Ecohydrological interactions in a degraded two-phase mosaic dryland: Implications for regime shifts, resilience, and restoration, *Ecohydrology*, doi:10.1002/eco.260, in press.
- Laio, F., A. Porporato, L. Ridolfi, and I. Rodriguez-Iturbe (2001), Plants in water-controlled ecosystems: active role in hydrologic processes and response to water stress—II. Probabilistic soil moisture dynamics, *Adv. Water Resour.*, 24(7), 707–723.
- Lefever, R., and O. Lejeune (1997), On the origin of tiger bush, *Bull. Math. Biol.*, 59(2), 263–294.
- Lejeune, O., M. Tlidi, and R. Lefever (2004), Vegetation spots and stripes: Dissipative structures in arid landscapes, *Int. J. Quant. Chem.*, 98(2), 261–271, doi:10.1002/qua.10878.
- LeVeque, R. J. (1992), *Numerical Methods for Conservation Laws*, 2nd ed., Birkhauser, Boston.
- Levin, S. A. (1998), Ecosystems and the biosphere as complex adaptive systems, *Ecosystems*, 1(5), 431–436.
- Ludwig, J. A., R. W. Eager, G. N. Bastin, V. H. Chewings, and A. C. Liedloff (2002), A leakiness index for assessing landscape function using remote sensing, *Landscape Ecol.*, 17(2), 157–171.
- Ludwig, J. A., R. W. Eager, A. C. Liedloff, G. N. Bastin, and V. H. Chewings (2006), A new landscape leakiness index based on remotely sensed ground-cover data, *Ecol. Indic.*, 6(2), 327–336, doi:10.1016/j.ecolind.2005.03.010.
- Ludwig, J. A., G. N. Bastin, V. H. Chewings, R. W. Eager, and A. C. Liedloff (2007), Leakiness: A new index for monitoring the health of arid and semiarid landscapes using remotely sensed vegetation cover and elevation data, *Ecol. Indic.*, 7(2), 442–454, doi:10.1016/j.ecolind.2006.05.001.
- Manfreda, S., T. M. Scanlon, and K. K. Caylor (2009), On the importance of accurate depiction of infiltration processes on modelled soil moisture and vegetation water stress, *Ecohydrology*, 3(2), 155–165.
- Manor, A., and N. M. Shnerb (2008), Facilitation, competition, and vegetation patchiness: From scale free distribution to patterns, *J. Theor. Biol.*, 253(4), 838–842, doi:10.1016/j.jtbi.2008.04.012.
- Meehl, G. A., et al. (2007), *Climate Change 2007: The Physical Science Basis. Contribution of Working Group I to the Fourth Assessment Report of the Intergovernmental Panel on Climate Change*, Cambridge Univ. Press, New York.
- Newman, B. D., B. P. Wilcox, S. R. Archer, D. D. Breshears, C. N. Dahm, C. J. Duffy, N. G. McDowell, F. M. Phillips, B. R. Scanlon, and E. R. Vivoni (2006), Ecohydrology of water-limited environments: A scientific vision, *Water Resour. Res.*, 42, W06302, doi:10.1029/2005WR004141.
- Otieno, D. O., M. W. T. Schmidt, J. I. Kinyamario, and J. Tenhunen (2005), Responses of *Acacia tortilis* and *Acacia xanthophloea* to seasonal changes in soil water availability in the savanna region of Kenya, *J. Arid Environ.*, 62(3), 377–400.
- Quinn, P., K. Beven, P. Chevallier, and O. Planchon (1991), The prediction of hillslope flow paths for distributed hydrological modeling using digital terrain models, *Hydrol. Processes*, 5(1), 59–79, doi:10.1002/hyp.3360050106.
- Reynolds, J. F., et al. (2007), Global desertification: Building a science for dryland development, *Science*, 316(5826), 847–851, doi:10.1126/science.1131634.
- Rietkerk, M., and J. Van de Koppel (2008), Regular pattern formation in real ecosystems, *Trends Ecol. Evol.*, 23(3), 169–175, doi:10.1016/j.tree.2007.10.013.
- Rietkerk, M., P. Ketner, L. Stroosnijder, and H. H. T. Prins (1996), Sahelian rangeland development; A catastrophe?, *J. Range Manage.*, 49(6), 512–519.
- Rodriguez-Iturbe, I., and A. Porporato (2004), *Ecohydrology of Water-Controlled Ecosystems*, 442 pp., Cambridge Univ. Press, New York.
- Saco, P. M., G. R. Willgoose, and G. R. Hancock (2007), Eco-geomorphology of banded vegetation patterns in arid and semi-arid regions, *Hydrol. Earth Syst. Sci.*, 11(6), 1717–1730.
- Sankaran, M., et al. (2005), Determinants of woody cover in African savannas, *Nature*, 438(7069), 846–849.
- Scanlon, T. M., K. K. Caylor, S. A. Levin, and I. Rodriguez-Iturbe (2007), Positive feedbacks promote power-law clustering of Kalahari vegetation, *Nature*, 449(7159), 209–212, doi:10.1038/nature06060.
- Schymanski, S. J., M. Sivapalan, M. L. Roderick, J. Beringer, and L. B. Hutley (2008), An optimality-based model of the coupled soil moisture and root dynamics, *Hydrol. Earth Syst. Sci.*, 12(3), 913–932.
- Scott, R. L., W. L. Cable, and K. R. Hultine (2008), The ecohydrologic significance of hydraulic redistribution in a semiarid savanna, *Water Resour. Res.*, 44, W02440, doi:10.1029/2007WR006149.

- Sole, R. (2007), Ecology—Scaling laws in the drier, *Nature*, 449(7159), 151–153, doi:10.1038/449151a.
- Stauffer, D., and A. Aharony (1985), *An Introduction to Percolation Theory*, Taylor and Francis, London.
- Thompson, S. E., G. G. Katul, and A. Porporato (2010), Role of microtopography in rainfall-runoff partitioning: An analysis using idealized geometry, *Water Resour. Res.*, 46, W07520, doi:10.1029/2009WR008835.
- Tromp-van Meerveld, H. J., and J. J. McDonnell (2006), On the interrelations between topography, soil depth, soil moisture, transpiration rates and species distribution at the hillslope scale, *Adv. Water Resour.*, 29(2), 293–310, doi:10.1016/j.advwatres.2005.02.016f.
- Turnbull, L., J. Wainwright, and R. E. Brazier (2008), A conceptual framework for understanding semi-arid land degradation: Ecohydrological interactions across multiple-space and time scales, *Ecohydrology*, 1(1), 23–34, doi:10.1002/eco.4.
- van Wijk, M. T., and I. Rodríguez-Iturbe (2002), Tree-grass competition in space and time: Insights from a simple cellular automata model based on ecohydrological dynamics, *Water Resour. Res.*, 38(9), 1179, doi:10.1029/2001WR000768.
- Vereecken, H., J. A. Huisman, H. Bogen, J. Vanderborght, J. A. Vrugt, and J. W. Hopmans (2008), On the value of soil moisture measurements in vadose zone hydrology: A review, *Water Resour. Res.*, 44, W00D06, doi:10.1029/2008WR006829.
- von Hardenberg, J., A. Y. Kletter, H. Yizhaq, J. Nathan, and E. Meron (2010), Periodic versus scale-free patterns in dryland vegetation, *Proc. R. Soc. B*, 277(1688), 1771–1776, doi:10.1098/rspb.2009.2208.
- Walpole, R. E., R. H. Myers, S. L. Myers, and K. Ye (2002), *Probability and Statistics for Engineers and Scientists*, 7th ed., Prentice Hall, Upper Saddle River, N. J.
- Wilcox, B. P., and B. D. Newman (2005), Ecohydrology of semiarid landscapes, *Ecology*, 86(2), 275–276.
- Williams, C. A., and J. D. Albertson (2004), Soil moisture controls on canopy-scale water and carbon fluxes in an African savanna, *Water Resour. Res.*, 40, W09302, doi:10.1029/2004WR003208.

---

K. K. Caylor, M. A. Celia, J. M. Nordbotten, and I. Rodríguez-Iturbe, Department of Civil and Environmental Engineering, Princeton University, E205 Engineering Quad, Princeton, NJ 08544, USA.

T. E. Franz, Department of Hydrology and Water Resources, University of Arizona, 1133 E James E Rogers Way, Room 122, Tucson, AZ 85721, USA. (tfranz@email.arizona.edu)

E. G. King, Department of Ecology and Evolutionary Biology, Princeton University, 106 Guyot Hall, Princeton, NJ 08544, USA.